

<sup>1</sup> Study of the multi-strange resonance  $\Xi(1530)^0$  production  
<sup>2</sup> with ALICE at the LHC energies

<sup>3</sup> Jihye Song

## **4** Contents

<b>5</b>	<b>List of Figures</b>	<b>4</b>
<b>6</b>	<b>List of Tables</b>	<b>7</b>
<b>7</b>	<b>1 The physics of relativistic heavy-ion collisions</b>	<b>8</b>
8	1.1 Standard model . . . . .	8
9	1.2 Quantum Chromo-Dynamics . . . . .	8
10	1.3 Heavy Ion Collisions . . . . .	8
<b>11</b>	<b>2 Production of resonance with strangeness</b>	<b>8</b>
12	2.1 Resonance with strangeness . . . . .	8
<b>13</b>	<b>3 Theoretical models</b>	<b>8</b>
14	3.1 Thermal statistical model . . . . .	8
15	3.1.1 Calculations . . . . .	10
16	3.1.2 Results . . . . .	10
17	3.1.3 Comparison with data . . . . .	12
18	3.2 UrQMD . . . . .	12
<b>19</b>	<b>4 A Large Ion Collider Experiment at the LHC</b>	<b>12</b>
20	4.1 The Large Hadron Collider . . . . .	13
21	4.2 The ALICE project . . . . .	13
22	4.2.1 ALICE detector . . . . .	13
23	4.2.2 Data Acquisition (DAQ) and trigger system . . . . .	13
24	4.2.3 ALICE offline software frame work . . . . .	13
<b>25</b>	<b>5 Measurement of <math>\Xi(1530)^0</math> production in p-Pb and Pb-Pb</b>	<b>13</b>
26	5.1 $\Xi(1530)^0$ -reconstruction . . . . .	14
27	5.1.1 Data sample and event selection . . . . .	14
28	5.1.2 Track and topological selection . . . . .	17
29	5.1.3 Particle identification . . . . .	20
30	5.1.4 Signal extraction . . . . .	23
31	5.2 Efficiency correction . . . . .	32
32	5.3 Corrected $p_T$ -spectra . . . . .	35
33	5.4 Systematic uncertainties . . . . .	37
34	5.5 $\Xi(1530)^0$ transverse momentum spectra . . . . .	42
<b>35</b>	<b>6 Results</b>	<b>45</b>
36	6.1 Mean transverse momentum . . . . .	45
37	6.2 Particle yield ratios . . . . .	47

38	6.2.1	Comparison with other resonances . . . . .	47
39	6.2.2	Comparison with models . . . . .	47
40	<b>References</b>		<b>47</b>

<sup>41</sup> **List of Figures**

42	1	Ratio of baryonic and mesonic resonances over their stable partner as a function of temperature. . . . .	11
44	2	Ratio of resonances over their stable partner as a function of $\sqrt(s)$ . . . . .	12
45	3	Vertex-z coordinate distribution of the accepted events in p–Pb collision(Left) and in Pb–Pb collisions(Right). The red dashed line indicates vertex cut . . . . .	15
47	4	Multiplicity distribution of accepted events in p–Pb collision in percentile. The each color and labels define the four intervals in which the analysis is performed. . . . .	16
50	5	Centrality distribution of three different trigger classes. . . . .	17
51	6	Sketch of the decay modes for $\Xi^{*0}$ and depiction of the track and topological selection criteria. . . . .	19
53	7	TPC $dE/dx$ as function of transverse momentum for total (top) and selected first emitted $\pi$ in $3\sigma$ (bottom) . . . . .	20
55	8	TPC $dE/dx$ as function of transverse momentum for total (top) and selected second emitted $\pi$ in $3\sigma$ (bottom) . . . . .	20
57	9	TPC $dE/dx$ as function of transverse momentum for total (top) and selected last emitted $\pi$ in $3\sigma$ (bottom) . . . . .	21
59	10	TPC $dE/dx$ as function of transverse momentum for total (top) and selected proton in $3\sigma$ (bottom) . . . . .	21
61	11	TPC $dE/dx$ as function of transverse momentum for total (top) and selected first emitted $\pi$ in $3\sigma$ (bottom) . . . . .	21
63	12	TPC $dE/dx$ as function of transverse momentum for total (top) and selected second emitted $\pi$ in $3\sigma$ (bottom) . . . . .	22
65	13	TPC $dE/dx$ as function of transverse momentum for total (top) and selected last emitted $\pi$ in $3\sigma$ (bottom) . . . . .	22
67	14	TPC $dE/dx$ as function of transverse momentum for total (top) and selected proton in $3\sigma$ (bottom) . . . . .	23
69	15	The $\Xi^\mp\pi^\pm$ invariant mass distribution (Same-event pairs) in $1.8 < p_T < 2.2 \text{ GeV}/c$ and for the multiplicity class 20-40%. The background shape, using pairs from different events (Mixed-event background), is normalised to the counts in $1.49 < M_{\Xi\pi} < 1.51 \text{ GeV}/c^2$ and $1.56 < M_{\Xi\pi} < 1.58 \text{ GeV}/c^2$ . . . . .	24
73	16	The $\Xi^\mp\pi^\pm$ invariant mass distribution (Same-event pairs) in $3.0 < p_T < 3.5 \text{ GeV}/c$ and for the centrality class 0-10%. The background shape, using pairs from different events (Mixed-event background), is normalised to the counts in $1.49 < M_{\Xi\pi} < 1.51 \text{ GeV}/c^2$ and $1.56 < M_{\Xi\pi} < 1.58 \text{ GeV}/c^2$ . . . . .	25
77	17	The invariant mass distribution after subtraction of the mixed-event background in p–Pb collisions. The solid curve represents the combined fit, while the dashed line describes the residual background. . . . .	26

80	18	The invariant mass distribution after subtraction of the mixed-event background in Pb–Pb collisions. The solid curve represents the combined fit, while the dashed line describes the residual background. . . . .	27
81	19	$\sigma$ fit parameters as a function of $p_{\text{T}}$ in MB in p–Pb collisions (top) and in Pb–Pb collisions (bottom). . . . .	29
82	20	$\Xi(1530)^0$ -mass obtained from fit of the Voigtian peak as a function of $p_{\text{T}}$ in each multiplicity classes in p–Pb collisions (top) and the different centrality classes in Pb–Pb (bottom). . . . .	30
83	21	$\Xi(1530)^0$ -raw spectra obtained from fit of the Voigtian peak and a polynomial residual background for different multiplicities in p–Pb collisions (top) and Pb–Pb collisions (bottom). Only the statistical error is reported. . . . .	31
84	22	$\Xi(1530)^0$ -raw spectra obtained from fit of the Voigtian peak and a polynomial residual background for different multiplicities. Only the statistical error is reported. . . . .	32
85	23	Real corrected $\Xi(1530)^0$ spectrum (black) for the minimum bias with Levy fit (black curve). Also shown are the unweighted generated (blue) and reconstructed (red) $\Xi(1530)^0$ spectra. . . . .	33
86	24	Efficiency as a function of $p_{\text{T}}$ in minimum bias events in p–Pb collisions. . . . .	34
87	25	Efficiency as a function of $p_{\text{T}}$ in different centrality classes in Pb–Pb collisions . . . . .	35
88	26	Corrected $p_{\text{T}}$ -spectra of $\Xi(1530)^0$ in NSD and different multiplicity classes in p–Pb collisions. . . . .	36
89	27	Corrected $p_{\text{T}}$ -spectra of $\Xi(1530)^0$ in different centrality classes in Pb–Pb collisions. . . . .	36
90	28	Summary of the contributions to the systematic uncertainty in minimum bias events in p–Pb collisions. The dashed black line is the sum in quadrature of all the contributions. . . . .	40
91	29	Systematic uncertainties for each multiplicity classes in p–Pb collisions. . . . .	40
92	30	Summary of the contributions to the systematic uncertainty in minimum bias events in Pb–Pb collisions. The dashed black line is the sum in quadrature of all the contributions. . . . .	41
93	31	Systematic uncertainties for each multiplicity classes. . . . .	41
94	32	Corrected yields as function of $p_{\text{T}}$ in NSD events and multiplicity dependent event classes in p–Pb collision system. Statistical uncertainties are presented as bar and systematical uncertainties are plotted as boxes. . . . .	43
95	33	Corrected yields as function of $p_{\text{T}}$ in different centrality classes in Pb–Pb collision system. Statistical uncertainties are presented as bar and systematical uncertainties are plotted as boxes. . . . .	44

117	34	Mean transverse momenta $\langle p_T \rangle$ of $\Lambda$ , $\Xi^-$ , $\Sigma^{*\pm}$ , $\Xi^{*0}$ and $\Omega^-$ in p–Pb collisions at $\sqrt{s_{\text{NN}}} = 5.02$ TeV as a function of mean charged-particle multiplicity density $\langle dN_{\text{ch}}/d\eta_{\text{lab}} \rangle$ , measured in the pseudorapidity range $ \eta_{\text{lab}}  < 0.5$ . The results for $\Lambda$ , $\Xi^-$ and $\Omega^-$ are taken from [1, 2, 3]. Statistical and systematic uncertainties are represented as bars and boxes, respectively. The $\Omega^-$ and $\Xi^-$ points in the 3rd and 4th lowest multiplicity bins are slightly displaced along the abscissa to avoid superposition with the $\Xi(1530)^0$ points. . . . .	45
118			
119			
120			
121			
122			
123			
124	35	Mass dependence of the mean transverse momenta of identified particles for the 0 – 20% V0A multiplicity class and with $-0.5 < y_{\text{CMS}} < 0$ in p–Pb collisions at $\sqrt{s_{\text{NN}}} = 5.02$ TeV [1, 3], and in minimum-bias pp collisions at $\sqrt{s} = 7$ TeV [4] with $ y_{\text{CMS}}  < 0.5$ . Additionally, $D^0$ and $J/\psi$ results are plotted. The $D^0$ and $J/\psi$ were measured in different rapidity ranges: $ y_{\text{CMS}}  < 0.5$ [5] ( $ y_{\text{CMS}}  < 0.9$ [6]) for $D^0$ ( $J/\psi$ ) in pp and $-0.96 < y_{\text{CMS}} < 0.04$ [5] ( $-1.37 < y_{\text{CMS}} < 0.43$ [7]) for $D^0$ ( $J/\psi$ ) in p–Pb. Note also that the results for $D^0$ and $J/\psi$ in p–Pb collisions are for the 0–100% multiplicity class. . . . .	46
125			
126			
127			
128			
129			
130			
131			
132	36	Integrated. . . . .	48
133	37	Integrated. . . . .	49
134			

<sup>135</sup> **List of Tables**

136	1	Parameters used in the thermal-model calculations. . . . .	9
137	2	Properties of particles used in the ratio calculations. . . . .	10
138	3	Difference of mass ( $\Delta M$ ), baryon number ( $\Delta B$ ), strangeness ( $\Delta S$ ) and charge ( $\Delta Q$ ) of the ratios. The values of the slopes needs to be checked!!!! .	12
139			
140	4	Number of accepted and analyzed events per multiplicity/centrality interval	17
141	5	Track selections common to all decay daughters and primary track selections applied to the charged pions from decays of $\Xi^{*0}$ . . . . .	18
142	6	Topological and track selection criteria. . . . .	18
143	7	Summary of the systematic uncertainties on the differential yield, $d^2N/(dp_T dy)$ . Minimum and maximum values in all $p_T$ intervals and multiplicity classes in p–Pb, centrality classes in Pb–Pb are shown for each source. . . . .	42
144			
145			
146			

147 **1 The physics of relativistic heavy-ion collisions**

148 This test for references [8]

149 **1.1 Standard model**

150 **1.2 Quantum Chromo-Dynamics**

151 **1.3 Heavy Ion Collisions**

152 **2 Production of resonance with strangeness**

153 **2.1 Resonance with strangeness**

154 **3 Theoretical models**

155 **3.1 Thermal statistical model**

156 The statistical-thermal model has proved extremely successful in applications to relativistic  
157 collisions of both heavy ions and elementary particles. In light of this success, THERMUS,  
158 a thermal model analysis package, has been developed for incorporation into the object-  
159 oriented ROOT framework [9].

160  
161 There are three types of statistical-thermal models in explaining data in high energy nu-  
162 clear physics and THERMUS treats the system quantum numbers B (baryon number), S  
163 (strangeness) and Q (charge) within three distinct formalisms:

164 1. **Grand-Canonical Ensemble:** Because the hot dense matter produced in nucleus-  
165 nucleus collisions is large enough, this ensemble is the most widely used in applications  
166 to heavy-ion collisions, in which the quantum numbers are conserved on average.

167 2. **Fully-Canonical Ensemble:** In which B, S and Q are each exactly conserved and  
168 this ensemble used in high-energy elementary collisions such as pp, p $\bar{p}$  and e $^-$ e $^+$   
169 collisions.

170 3. **Strangeness-Canonical Ensemble:** In small systems or at low temperatures, a  
171 canonical treatment leads to a suppression of hadrons carrying non-zero quantum  
172 numbers, since these particles have to be created in pairs and the resulting low  
173 production of strange particles requires a canonical treatment of strangeness.

174 In order to calculate the thermal properties of a system, one starts with an evaluation  
175 of its partition function. The form of the partition function obviously depends on the  
176 choice of ensemble. In the present analysis the strangeness-canonical ensemble used and  
177 the statistical-thermal model requires six parameters as input: the chemical freeze-out

178 temperature  $T$ , baryon and charge chemical potentials  $\mu_B$  and  $\mu_Q$  respectively, canonical  
179 or correlation radius,  $R_C$ ; the radius inside which strangeness is exactly conserved and the  
180 fireball radius  $R$ . An additional strangeness saturation factor  $\gamma_S$  has been used as indicator  
181 of a possible departure from equilibrium and  $\gamma_S = 1.0$  corresponds to complete strangeness  
182 equilibration.

183 The volume dependence cancels out when studying the particle ratios as well as strangeness  
184 canonical equivalent to grand canonical formalism if  $\Delta S = 0$  in the ratios and  $\gamma_S$  also can-  
185 cels out. Parameters used in the analysis listed in Table 1. The  $\mu_B$  parameter taken from  
186 the Ref. [10].

Table 1: Parameters used in the thermal-model calculations.

Parameter	Value
$T$ (MeV)	varied (see text)
$\mu_B$ (MeV)	$9.2 \times 10^{-2}????$
$\mu_Q$ (MeV)	0.0
$\gamma_S$	1.0

188 **3.1.1 Calculations**

189 *Concept:*

190 In order to calculate the particle ratios within strangeness canonical formalism of THER-  
 191 MUS, temperature varied between 60 MeV to 180 MeV and particle yields extracted for  
 192 each temperature value and then primary particle ratios calculated for each case.

193

194 *Feed-Down Correction:*

195 Since the particle yields measured by the detectors in collision experiments include feed-  
 196 down from heavier hadrons and hadronic resonances, the primordial hadrons are allowed to  
 197 decay to particles considered stable by the experiment before model predictions are com-  
 198 compared with experimental data. In the analysis only  $\Lambda$  particles counted as stable (do not  
 199 allowed to decay) so there is no feed-down contribution from these particles to the other  
 200 ratios.

201

202

203 Properties of studied particles and their particle ratios listed in Table 2 and Table 3,  
 204 respectively.

Table 2: Properties of particles used in the ratio calculations.

Particle	$\Delta^{++}$	p	$K^{*0}$	$K^0$	$K^+$	$\Lambda^*$	$\Lambda$	$\Sigma^{*+}$	$\Sigma^+$	$\Sigma^0$
Mass ( $MeV/c^2$ )	1232	938.27	895.92	497.61	493.67	1519.5	1115.68	1382.8	1189.37	1192.6
Width ( $MeV/c^2$ )	120	–	50.7	–	–	15.6	–	37.6	–	–
$c\tau$ (fm)	1.6	–	3.9	–	–	12.6	–	5.51	–	–
Ang. Momentum ( $J$ )	3/2	1/2	1	1	0	3/2	1/2	3/2	1/2	1/2
Isospin ( $I$ )	3/2	1/2	1/2	1/2	1/2	0	0	1	1	1
Parity ( $P$ )	+1	+1	-1	-1	0	-1	+1	+1	+1	+1
Strangeness ( $S$ )	0	0	1	1	1	-1	-1	-1	-1	-1
Baryon Number ( $B$ )	1	1	0	0	0	1	1	1	1	1
Decay Channel	$p\pi^+$	–	$\pi^-$	–	$\mu^+\nu_\mu$	$pK^-$	$p\pi^-$	$\Lambda\pi^+$	$p\pi^0$	$\Lambda\gamma$
Branching Ratio (%)	~ 100	–	~ 66.7	–	~ 63.54	~ 45	~ 63.9	~ 87	~ 51.6	~ 100
Q-Value( $MeV/c^2$ )	154.16	–	262.68	–	–	87.55	37.84	127.55	111.53	76.96

205

206

207 **3.1.2 Results**

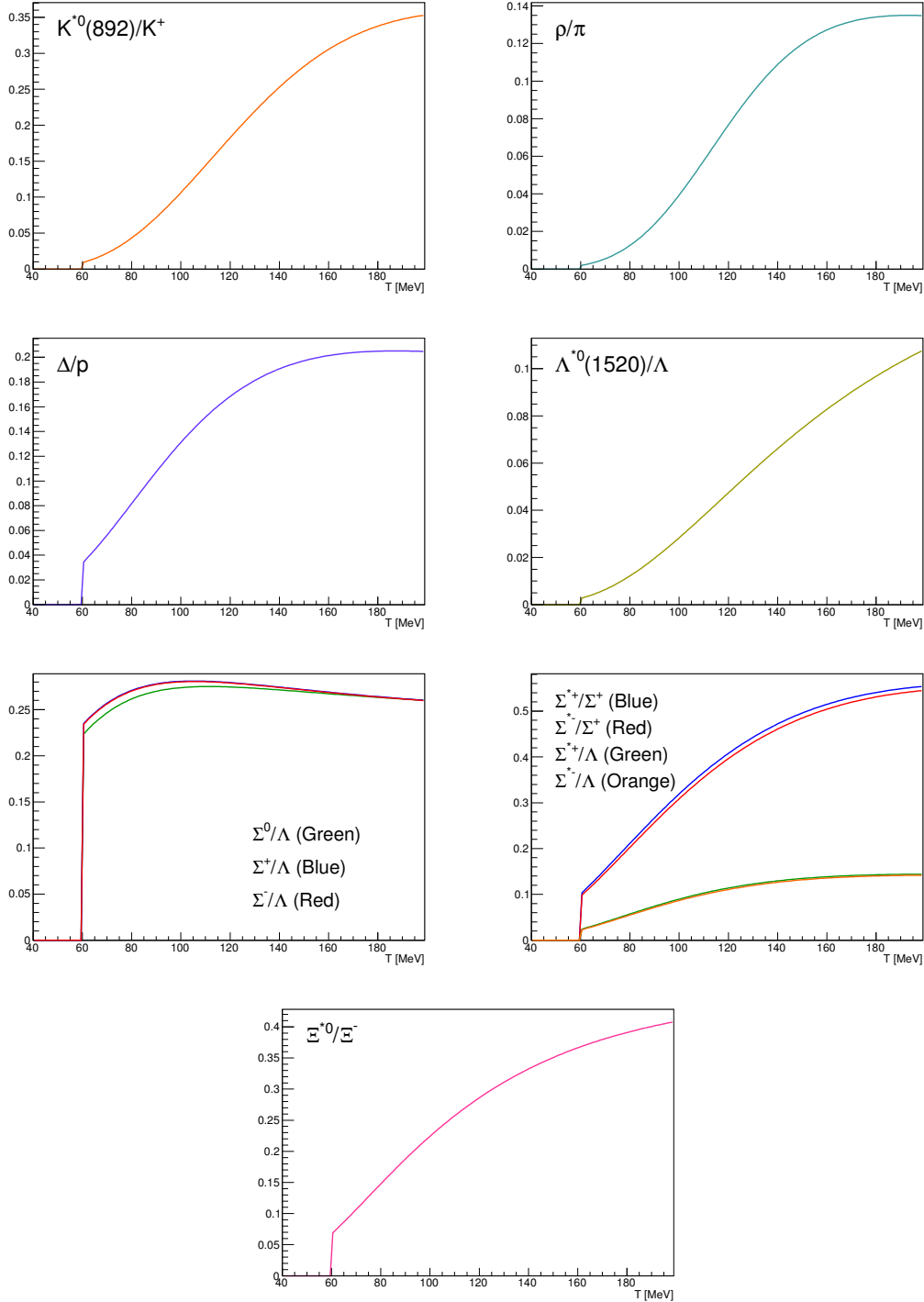


Figure 1: Ratio of baryonic and mesonic resonances over their stable partner as a function of temperature.

Table 3: Difference of mass ( $\Delta M$ ), baryon number ( $\Delta B$ ), strangeness ( $\Delta S$ ) and charge ( $\Delta Q$ ) of the ratios. The values of the slopes needs to be checked!!!!

Particle	$\Delta^{++}/p$	$K^*/K^+$	$\Lambda^*/\Lambda$	$\Sigma^{*+}/\Lambda$	$\Sigma^{*+}/\Sigma^0$	$\Sigma^0/\Lambda$	$\Sigma^{*+}/\Sigma^+$	$\Xi^{*0}/\Xi^-$
$\Delta M$ (MeV/ $c^2$ )	293.8	402.25	403.82	267.12	190.16	76.96	193.43	210.49
$\Delta B$	0	0	0	0	0	0	0	0
$\Delta S$	0	0	0	0	0	0	0	0
$\Delta Q$	+1	-1	0	+1	0	+1	0	-1
Slope (%) per MeV ????????	0.19	0.76	0.98	0.25	-	-0.08	0.37	0.42

### 208 3.1.3 Comparison with data

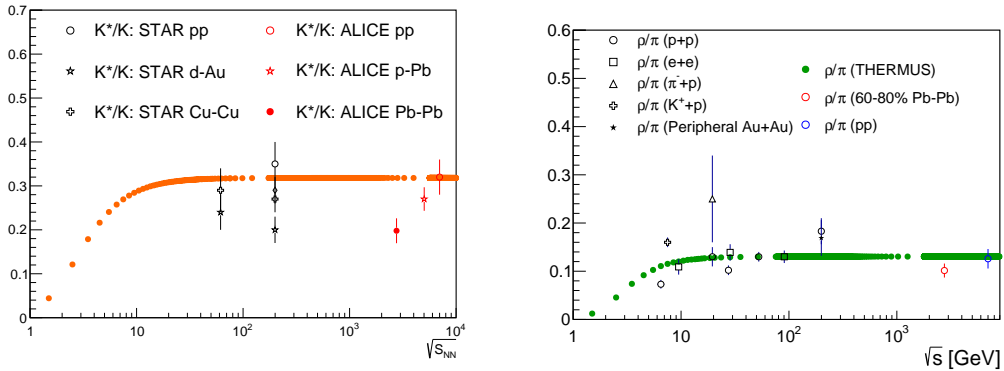


Figure 2: Ratio of resonances over their stable partner as a function of  $\sqrt{(s)}$ .

### 209 3.2 UrQMD

## 210 4 A Large Ion Collider Experiment at the LHC

211 ALICE (A Large Ion Collider Experiment) has been collecting data during the whole first  
 212 phase of the Large Hadron Collider operations, from its startup on the 23 November 2009  
 213 to the beginning of the first long technical shutdown in February 2013. During the first  
 214 three years of operations LHC provided pp collisions at 0.9, 2.76, 7 and 8 TeV, Pb?Pb  
 215 collisions at 2.76A TeV and finally p?Pb collisions at 5.02 TeV. The first section of this  
 216 chapter focuses on the LHC performance during this phase and includes details on the  
 217 accelerator parameters that allow the LHC to perform as a lead ion collider. A detailed  
 218 description of the ALICE detector follows in the section 2.2. ALICE has been designed and

219 optimized to study the high particle-multiplicity environment of ultra-relativistic heavy-ion  
220 collisions and its tracking and particle identification performance in Pb-Pb collisions are  
221 discussed. The attention is drawn in particular on the central barrel detectors. Section  
222 2.3 de- scribes the ALICE Data Acquisition (DAQ) system, that also embeds tools for the  
223 online Data Quality Monitoring (DQM). The final part of the chapter is dedicated to the  
224 offline computing and reconstruction system based on the GRID framework.

225 **4.1 The Large Hadron Collider**

226 The Large Hadron Collider (LHC) [57], [58] is a two-ring-superconducting hadron accel-  
227 erator and collider installed in the 26.7 Km tunnel that hosted the LEP ma- chine and it  
228 completes the CERN accelerator complex together with the PS and SPS, among the others  
229 shown in fig. 2.1. Four main experiments are located in four different interaction points  
230 along its circumference. ATLAS and CMS, the biggest ones, are multi-purpose detectors  
231 built to discover the Higgs boson and hints of new physics beyond the Standard Model.  
232 LHCb is dedicated to the physics of the flavour, focusing on the study CP-violation using B  
233 meson decay channels. The phenomena that these three experiments aim to observe have  
234 production cross sec- tion of the order of a hundred of pb or lower, therefore a large number  
235 of collision events is required to the machine in order to fulfill the LHC pp physics program.  
236 ALICE, on the contrary, is dedicated to the physics of Quark Gluon Plasma through the  
237 observation of high-energy heavy-ion collisions, although a shorter physics pro- gram with  
238 pp collisions has been carried out.

229 **4.2 The ALICE project**

240 **4.2.1 ALICE detector**

241 **4.2.2 Data Acquisition (DAQ) and trigger system**

242 **4.2.3 ALICE offline software frame work**

243 **5 Measurement of  $\Xi(1530)^0$  production in p–Pb and Pb–Pb**

244 The measurement of resonance production in p–Pb collisions helps to disentangle cold  
245 nuclear matter effects from genuine hot medium effects and contribute to the study of  
246 the system size dependence of re-scattering in the hadronic phase. And the measurement  
247 in ultra-relativistic heavy-ion collisions such as Pb–Pb collisions, provide information on  
248 the properties of hadronic medium and different stage of its evolution. In order to study  
249 the particle production mechanism in the hadronic phase between the chemical and ki-  
250 netic freeze-out, the  $\Xi(1530)^0$  resonance production at mid-rapidity( $-0.5 < y_{\text{CMS}} < 0$ ) is  
251 measured in p–Pb collisions  $\sqrt{s_{\text{NN}}} = 5.02$  TeV and in Pb–Pb collisions with  $|y| < 0.5$  at  
252  $\sqrt{s_{\text{NN}}} = 2.76$  TeV with the ALICE experiment, via the reconstruction of its hadronic decay  
253 into  $\Xi\pi$ .

254 **5.1  $\Xi(1530)^0$  -reconstruction**

255 The  $\Xi^{*0}$  production in p–Pb and Pb–Pb collisions at mid-rapidity has been studied in dif-  
256 ferent multiplicity classes, from very central to peripheral collisions. The analysis strategy  
257 is based on the invariant mass study of the reconstructed pairs (referred to as the candi-  
258 dates) whose provenance could be the decay of a  $\Xi^{*0}$  baryon into charged particles. The  
259 decay products (also called daughters in the text) are identified as oppositely charged  $\Xi$  and  
260  $\pi$  among the tracks reconstructed in the central barrel. The event selection, track selec-  
261 tion and the particle identification strategy is described. The raw signal yield is extracted  
262 by fitting the background-subtracted invariant mass distribution in several transverse mo-  
263 mentum intervals. In order to extract the  $p_T$ -dependent cross section, these yields are  
264 corrected for efficiency. The  $p_T$ -dependent correction due to the detector acceptance and  
265 reconstruction efficiency,  $(\text{Acc} \times \epsilon_{rec})(p_T)$ , is computed from a Monte Carlo simulation.  
266 The absolute normalisation is then performed, by dividing for the number of the events in  
267 each multiplicity and centrality classes.

268 **5.1.1 Data sample and event selection**

269 A description of the ALICE detector and of its performance during the LHC Run 1 (2010–  
270 2013) can be found in [11, 12]. The data sample in the analysis from Pb–Pb collisions with  
271 energy of  $\sqrt{s_{\text{NN}}}=2.76$  obtained during 2011 and the sample of p–Pb run at  $\sqrt{s_{\text{NN}}}=5.02$   
272 TeV was recorded in 2013.

273 Due to the asymmetric energies of the proton (4 TeV) and lead ion (1.57 A TeV) beams,  
274 the centre-of-mass system in the nucleon-nucleon frame is shifted in rapidity by  $\Delta y_{\text{NN}} =$   
275 0.465 towards the direction of the proton beam with respect to the laboratory frame of  
276 the ALICE detector [2]. For the analysed p–Pb data set, the direction of the proton beam  
277 was towards the ALICE muon spectrometer, the so-called “C” side, standing for negative  
278 rapidities; conversely, the Pb beam circulated towards positive rapidities, labelled as “A”  
279 side in the following. The analysis in this paper was carried out at midrapidity, in the  
280 rapidity window  $-0.5 < y_{\text{CMS}} < 0$ .

281 The minimum-bias trigger during the p–Pb run was configured to select events by  
282 requiring a logical OR of signals in V0A and V0C [12], two arrays of 32 scintillator detectors  
283 covering the full azimuthal angle in the pseudo-rapidity regions  $2.8 < \eta_{\text{lab}} < 5.1$  and  
284  $-3.7 < \eta_{\text{lab}} < -1.7$ , respectively [13]. In the data analysis it was required to have a  
285 coincidence of signals in both V0A and V0C in order to reduce the contamination from  
286 single-diffractive and electromagnetic interactions. Out of this sample in p–Pb collision  
287 events about 109.3 million events, 93.9 million events satisfy the following selection criteria  
288 and have been actually used for the analysis.

289 The Pb–Pb collisions data sample was selected by online centrality trigger requiring a  
290 signal in the forward V0 detectors[14] to record enhanced data in central collision. The  
291 data consists of 24.8 million events in most central collisions (0-10%), 21.8 million events in  
292 semi-central collisions (10-50%) and 3.5 million events with minimum-bas trigger (0-90%).

293 Among 49.6 million events in total, 43.0 million events have been analyzed as passed the  
 294 criteria below.

- 295 • Events with z-coordinate of primary vertex ( $V_z$ ) falling within  $\pm 10$  cm from the  
 296 interaction point
- 297 • Rejection of pile-up event
- 298 • Requiring primary tracks to have at least one hit in one of the two innermost layers  
 299 of the ITS (silicon pixel detector, SPD)
- 300 • p–Pb: multiplicity ranges in percentile (V0A): 0-20%, 20-40%, 40-60%, 60-100% and  
 301 MB(0-100%)
- 302 • Pb–Pb: centrality classes (V0A and V0C): 0-10%, 10-40%, 40-80% and MB (0-80%)

303 The distribution of the vertex z position of the accepted events in p–Pb collision is  
 304 reported on left panel in Figure 3 and corresponding figure but obtained from Pb–Pb  
 305 collisions is shown on right panel in Figure. 3. Events with  $|V_z| < 10$  cm have been used  
 306 to ensure a uniform acceptance in the central pseudo-rapidity region,  $|\eta| < 0.8$ , where the  
 307 analysis is performed. This cut reduces the total number of events to 97.5 million events,  
 308 that is the  $\sim 89.2\%$  of the initial sample in p–Pb collisions and 43.04 million events which  
 309 is  $\sim 86.8\%$  of the initial sample in Pb–Pb collisions are survived.

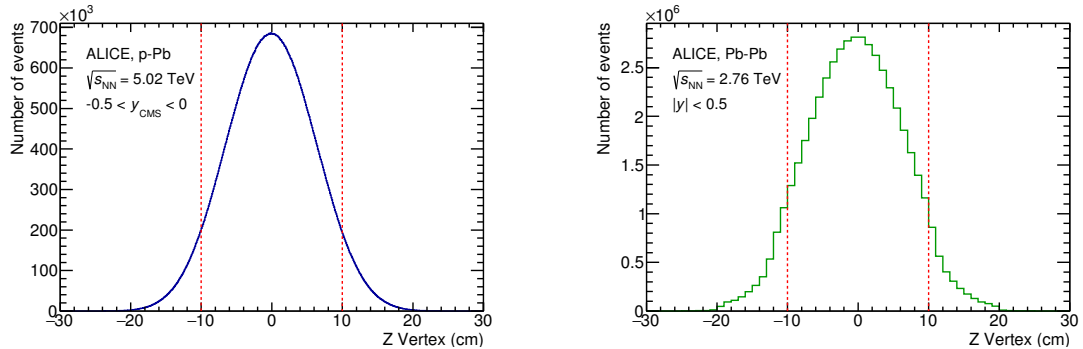


Figure 3: Vertex-z coordinate distribution of the accepted events in p–Pb collision(Left) and in Pb–Pb collisions(Right). The red dashed line indicates vertex cut

310 Fig. 4 shows the multiplicity distribution of the accepted events in p–Pb collision  
 311 divided in bins of percentile. The each color on the histogram indicate the multiplicity  
 312 ranges used in this analysis. Corresponding events for each multiplicity range are in Table  
 313 4.

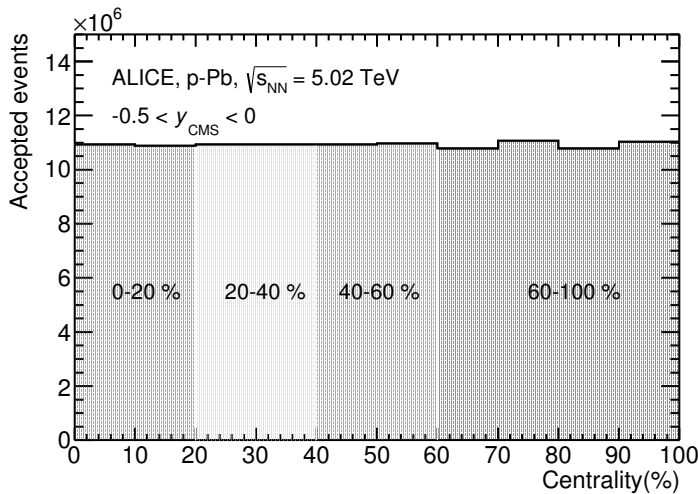


Figure 4: Multiplicity distribution of accepted events in p–Pb collision in percentile. The each color and labels define the four intervals in which the analysis is performed.

314     The distribution of centrality in each trigger used to select the events in Pb–Pb collision  
 315     is shown in Fig. 5 and the reason why the centrality has step structure is that there are  
 316     three different trigger classes classified by the amplitude threshold on VZERO detector.  
 317     Because the distribution of events as function of centrality is not a flat, this may lead to  
 318     additional bias, in particular when one needs to combine the results from different triggers.  
 319     For example, events from 40-80% centrality bin have bias with high statistics in 40-60%. In  
 320     order to avoid this effect, we have applied a flattening procedure to have flat distribution  
 321     of events as function of centrality. A brief explanation of the method is below :

- 322     1. Histograms are obtained for the effective mass distribution in 1% centrality bins and  
 323       for the centrality distribution  
  
 324     2. The effective mass distributions are scaled in each 1% centrality bin by a factor:  
 325       Factor = Nevent in 20-40% / 20 / Nevent in current 1% bin  
  
 326     3. Each bin in the centrality distribution is scaled using the factor described above  
  
 327     4. Histograms are added for centrality bins of interest: 0-10%, 10-40%, 40-80%, 0-80%

328     The resulting number of events in each centrality classes is summarized in Table 4.

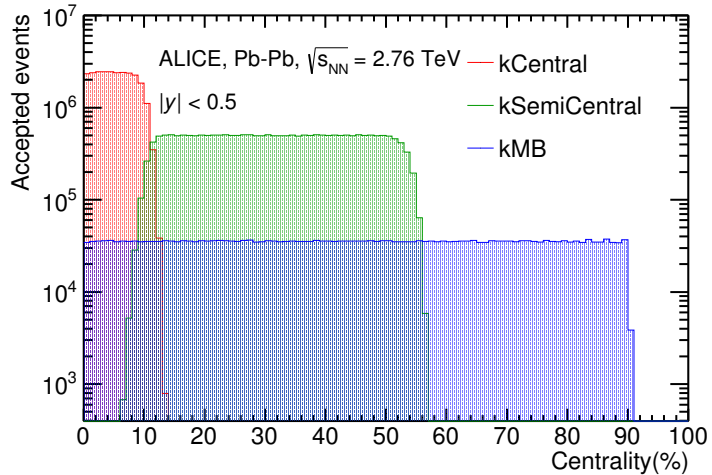


Figure 5: Centrality distribution of three different trigger classes.

p-Pb	0-20%	$21.82 \times 10^6$
	20-40%	$21.86 \times 10^6$
	40-60%	$21.91 \times 10^6$
	60-100%	$43.68 \times 10^6$
Pb-Pb	0-10%	$5.58 \times 10^6$
	10-40%	$16.73 \times 10^6$
	40-80%	$22.31 \times 10^6$

Table 4: Number of accepted and analyzed events per multiplicity/centrality interval

### 329 5.1.2 Track and topological selection

330 In comparison with the  $\Xi^{*0}$  analysis carried out in pp collisions at  $\sqrt{s} = 7$  TeV [4], track  
 331 and topological selections were revised and adapted to the p-Pb dataset. Pions from strong  
 332 decays of  $\Xi^{*0}$  were selected according to the criteria for primary tracks. As summarized  
 333 in Table 5, all charged tracks were selected with  $p_T > 0.15$  GeV/c and  $|\eta_{\text{lab}}| < 0.8$ ,  
 334 as described in Ref. [12]. The primary tracks were chosen with the Distance of Closest  
 335 Approach (DCA) to PV of less than 2 cm along the longitudinal direction ( $\text{DCA}_z$ ) and  
 336 lower than  $7\sigma_r$  in the transverse plane ( $\text{DCA}_r$ ), where  $\sigma_r$  is the resolution of  $\text{DCA}_r$ . The  $\sigma_r$   
 337 is strongly  $p_T$ -dependent and lower than 100  $\mu\text{m}$  for  $p_T > 0.5$  GeV/c [12]. To ensure a good  
 338 track reconstruction quality, candidate tracks were required to have at least one hit in one  
 339 of the two innermost layers (SPD) of the ITS and to have at least 70 reconstructed points in

<sup>340</sup> the Time Projection Chamber (TPC), out of a maximum of 159. The Particle IDentification  
<sup>341</sup> (PID) criteria for all decay daughters are based on the requirement that the specific energy  
<sup>342</sup> loss ( $dE/dx$ ) is measured in the TPC within three standard deviations ( $\sigma_{\text{TPC}}$ ) from the  
expected value ( $dE/dx_{\text{exp}}$ ), computed using a Bethe-Bloch parametrization [12].

Common track selections	$ \eta_{\text{lab}} $	$< 0.8$
	$p_T$	$> 0.15 \text{ GeV}/c$
	PID $ (\text{d}E/\text{d}x) - (\text{d}E/\text{d}x)_{\text{exp}} $	$< 3 \sigma_{\text{TPC}}$
Primary track selections	$\text{DCA}_z$ to PV	$< 2 \text{ cm}$
	$\text{DCA}_r$ to PV	$< 7\sigma_r - 10\sigma_r (p_T)$
	number of SPD points	$\geq 1$
	number of TPC points	$> 70$
	$\chi^2$ per cluster	$< 4$

Table 5: Track selections common to all decay daughters and primary track selections applied to the charged pions from decays of  $\Xi^{*0}$ .

<sup>343</sup> Since pions and protons from weak decay of  $\Lambda$  ( $c\tau = 7.89 \text{ cm}$  [15]) and pions from weak  
<sup>344</sup> decay of  $\Xi^-$  ( $c\tau = 4.91 \text{ cm}$  [15]) are produced away from the PV, specific topological and  
<sup>345</sup> track selection criteria, as summarized in Table 6, were applied [3, 4, 16].

Topological cuts	p–Pb	Pb–Pb
$\text{DCA}_r$ of $\Lambda$ decay products to PV	$> 0.06 \text{ cm}$	$> 0.11 \text{ cm}$
DCA between $\Lambda$ decay products	$< 1.4 \text{ cm}$	$< 0.95 \text{ cm}$
DCA of $\Lambda$ to PV	$> 0.015 \text{ cm}$	$> 0.06$
$\cos\theta_\Lambda$	$> 0.875$	$> 0.998$
$r(\Lambda)$	$0.2 < r(\Lambda) < 100 \text{ cm}$	$0.2 < r(\Lambda) < 100 \text{ cm}$
$ M_{p\pi} - m_\Lambda $	$< 7 \text{ MeV}/c^2$	$< 7 \text{ MeV}/c^2$
$\text{DCA}_r$ of pion (from $\Xi^-$ ) to PV	$> 0.015 \text{ cm}$	$> 0.035 \text{ cm}$
DCA between $\Xi^-$ decay products	$< 1.9 \text{ cm}$	$< 0.275$
$\cos\theta_\Xi$	$> 0.981$	$> 0.9992$
$r(\Xi^-)$	$0.2 < r(\Xi^-) < 100 \text{ cm}$	$0.2 < r(\Xi^-) < 100 \text{ cm}$
$ M_{\Lambda\pi} - m_\Xi $	$< 7 \text{ MeV}/c^2$	$< 7 \text{ MeV}/c^2$

Table 6: Topological and track selection criteria.

<sup>347</sup> In the analysis of  $\Xi^{*0}$ ,  $\Lambda$  and  $\pi$  from  $\Xi^-$  were selected with a DCA of less than 1.9 cm  
<sup>348</sup> and with a  $\text{DCA}_r$  to the PV greater than 0.015 cm. The  $\Lambda$  daughter particles ( $\pi$  and p)  
<sup>349</sup> were required to have a  $\text{DCA}_r$  to the PV greater than 0.06 cm, while the DCA between the  
<sup>350</sup> two particles was required to be less than 1.4 cm. Cuts on the invariant mass, the cosine

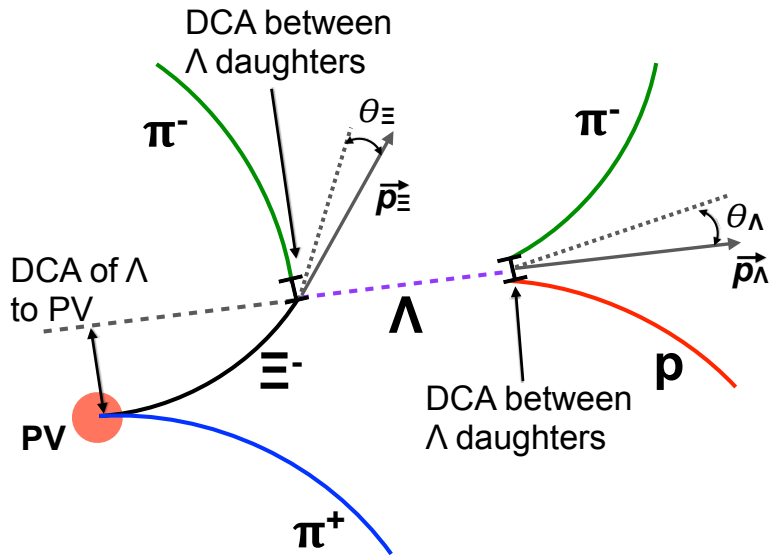


Figure 6: Sketch of the decay modes for  $\Xi^{*0}$  and depiction of the track and topological selection criteria.

<sup>351</sup> of the pointing angle ( $\theta_\Lambda, \theta_\Xi$ ) and the radius of the fiducial volume ( $r(\Lambda), r(\Xi)$ ) in Table 6  
<sup>352</sup> were applied to optimize the balance of purity and efficiency of each particle sample.

353 **5.1.3 Particle identification**

354 PID selection criteria are applied for

- 355 1.  $\pi^\pm$  (last emitted  $\pi$ ) and proton from  $\Lambda$
- 356 2.  $\pi^\pm$  (second emitted  $\pi$ ) from  $\Xi^\pm$
- 357 3.  $\pi^\pm$  (first emitted  $\pi$ ) from  $\Xi(1530)^0$

358 by using TPC. On TPC dE/dx versus momentum distribution,  $3\sigma$  cuts are applied to TPC  
 359 for selecting each of the particles. The TPC dE/dx selection allows to have better signal  
 360 with  $\sim 20\%$  increase of significance.

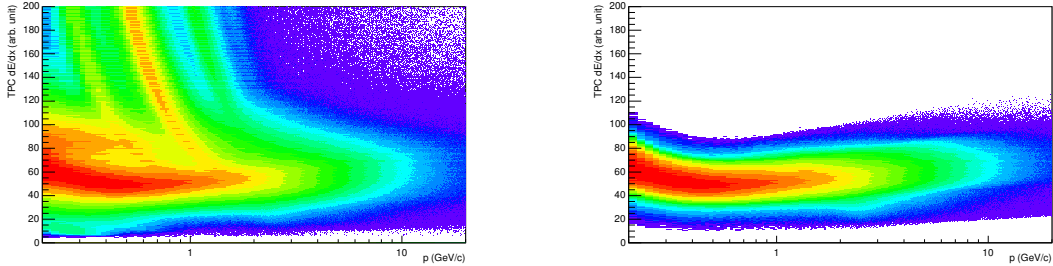


Figure 7: TPC dE/dx as function of transverse momentum for total (top) and selected first emitted  $\pi$  in  $3\sigma$  (bottom)

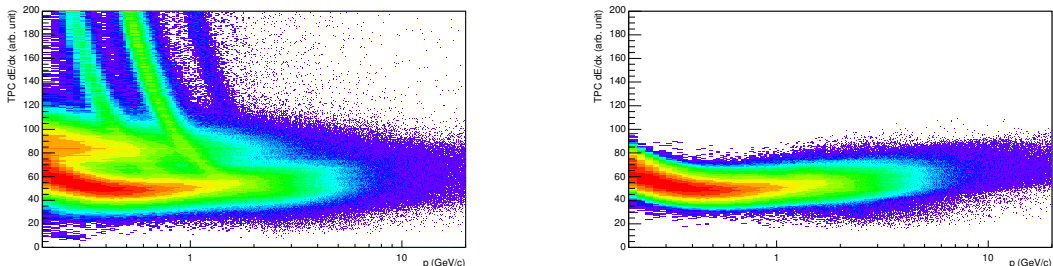


Figure 8: TPC dE/dx as function of transverse momentum for total (top) and selected second emitted  $\pi$  in  $3\sigma$  (bottom)

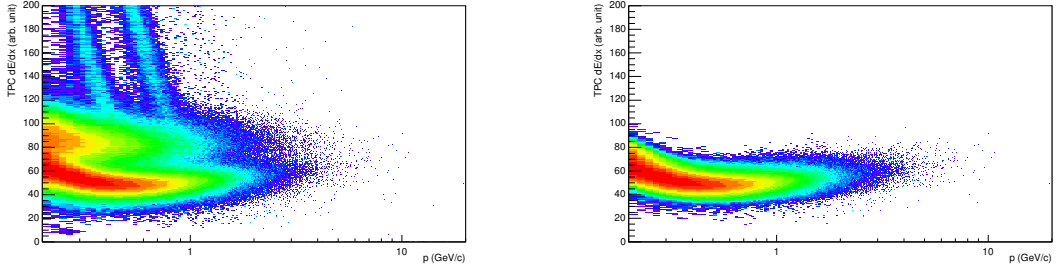


Figure 9: TPC  $dE/dx$  as function of transverse momentum for total (top) and selected last emitted  $\pi$  in  $3\sigma$ (bottom)

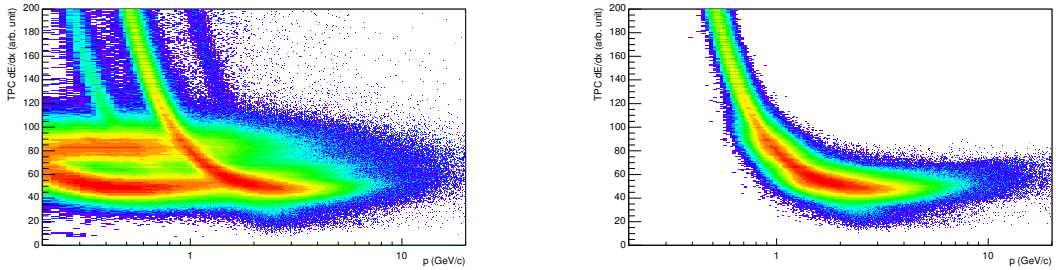


Figure 10: TPC  $dE/dx$  as function of transverse momentum for total (top) and selected proton in  $3\sigma$ (bottom)

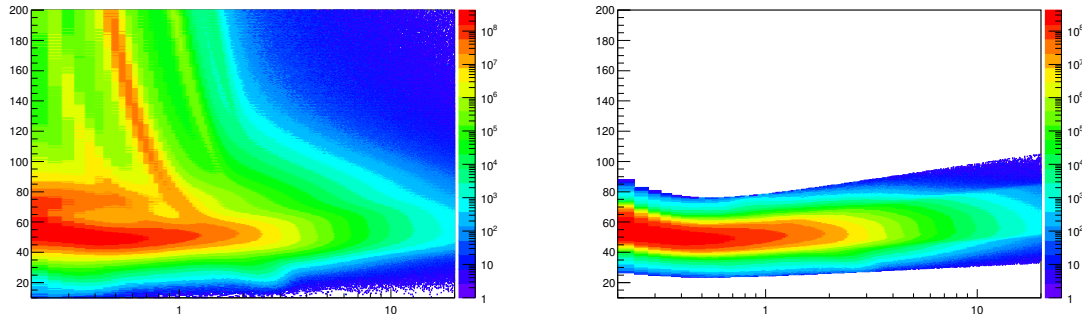


Figure 11: TPC  $dE/dx$  as function of transverse momentum for total (top) and selected first emitted  $\pi$  in  $3\sigma$  (bottom)

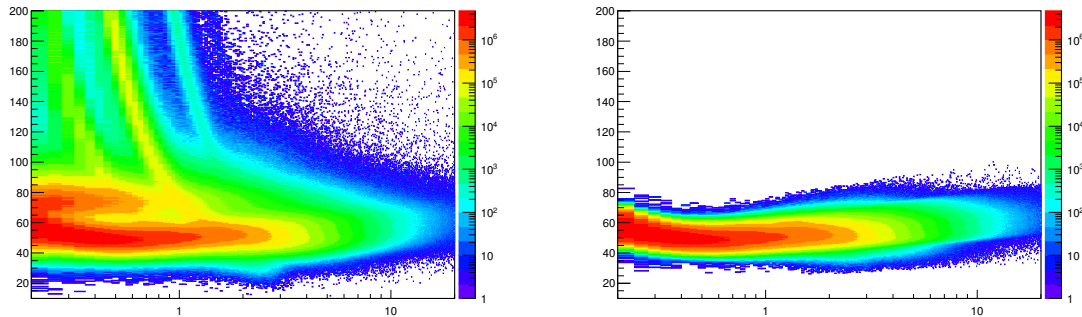


Figure 12: TPC  $dE/dx$  as function of transverse momentum for total (top) and selected second emitted  $\pi$  in  $3\sigma$ (bottom)

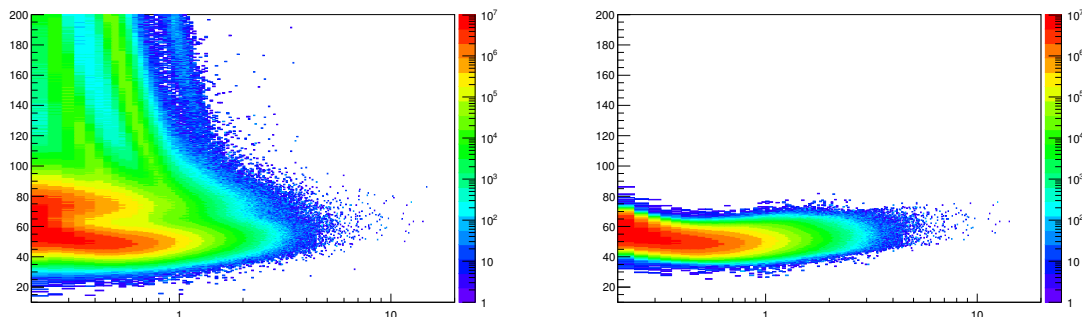


Figure 13: TPC  $dE/dx$  as function of transverse momentum for total (top) and selected last emitted  $\pi$  in  $3\sigma$ (bottom)

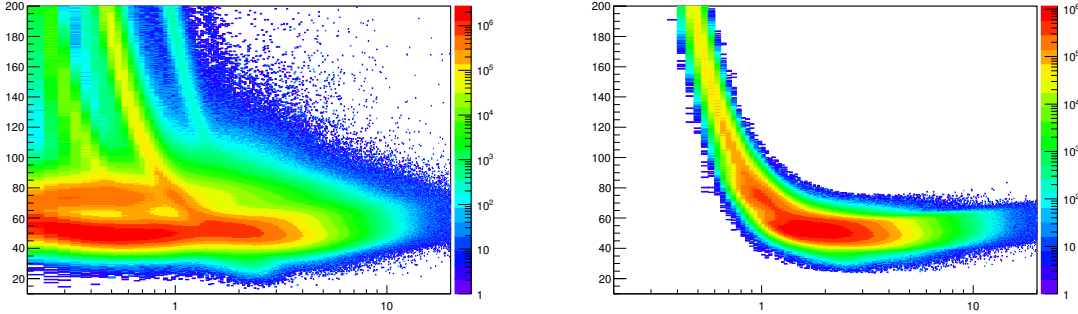


Figure 14: TPC  $dE/dx$  as function of transverse momentum for total (top) and selected proton in  $3\sigma$ (bottom)

### 361 5.1.4 Signal extraction

362 The  $\Xi^{*0}$  signals were reconstructed by invariant-mass analysis of candidates for the decay  
 363 products in each transverse momentum interval of the resonance particle, and for each  
 364 multiplicity class. The  $\Xi^-\pi^+(\Xi^+\pi^-)$  invariant mass distribution is reported in Figure 5.1.4  
 365 for semi-central events (20-40%) in p-Pb collisions and Figure 5.1.4 for central events(0-  
 366 10%) in Pb-Pb collisions.

367 Since the resonance decay products originate from a position which is indistinguishable  
 368 from the PV, a significant combinatorial background is present. In order to extract  
 369  $\Xi(1530)^0$  signal it is necessary to remove or, at least reduce, the combinatorial background.  
 370 For this analysis, this has been done with the event mixing (EM) technique, by combining  
 371 uncorrelated decay products 20 different events in p-Pb (5 different events in Pb-Pb). The  
 372 events for the mixing have been selected by applying the similarity criteria to minimise  
 373 distortions due to different acceptances and to ensure a similar event structure, only tracks  
 374 from events with similar vertex positions  $z$  ( $|\Delta z| < 1$  cm) and track multiplicities  $n$  ( $|\Delta n| <$   
 375 10) were taken.

376 The mixed-event background distributions were normalised to two fixed regions,  
 377  $1.49 < M_{\Xi\pi} < 1.51 \text{ GeV}/c^2$  and  $1.56 < M_{\Xi\pi} < 1.58 \text{ GeV}/c^2$ , around the  $\Xi^{*0}$  mass  
 378 peak (Figure 5.1.4 and 5.1.4). These regions were used for all  $p_T$  intervals and multiplicity  
 379 classes, because the background shape is reasonably well reproduced in these regions and  
 380 the invariant-mass resolution of the reconstructed peaks appears stable, independently of  
 381  $p_T$ . The uncertainty on the normalisation was estimated by varying the normalisation  
 382 regions and is included in the quoted systematic uncertainty for the signal extraction (Section 5.4).

384 After the background subtraction, the resulting distribution is shown in Figure 5.1.4  
 385 and 5.1.4. In order to obtain raw yields, a combined fit of a first-order polynomial for

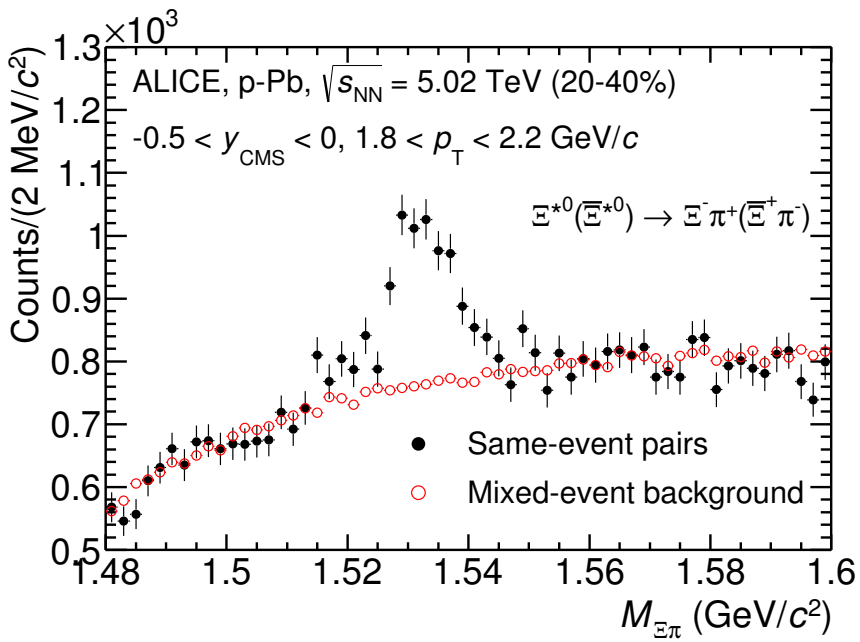


Figure 15: The  $\Xi^\mp\pi^\pm$  invariant mass distribution (Same-event pairs) in  $1.8 < p_{\text{T}} < 2.2 \text{ GeV}/c$  and for the multiplicity class 20-40%. The background shape, using pairs from different events (Mixed-event background), is normalised to the counts in  $1.49 < M_{\Xi\pi} < 1.51 \text{ GeV}/c^2$  and  $1.56 < M_{\Xi\pi} < 1.58 \text{ GeV}/c^2$ .

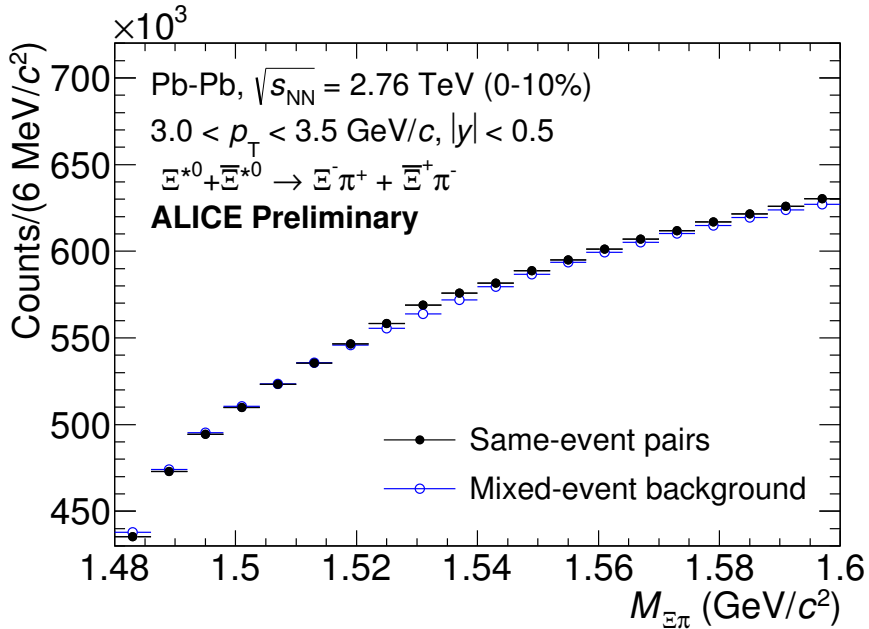


Figure 16: The  $\Xi^\pm \pi^\pm$  invariant mass distribution (Same-event pairs) in  $3.0 < p_T < 3.5 \text{ GeV}/c$  and for the centrality class 0-10%. The background shape, using pairs from different events (Mixed-event background), is normalised to the counts in  $1.49 < M_{\Xi\pi} < 1.51 \text{ GeV}/c^2$  and  $1.56 < M_{\Xi\pi} < 1.58 \text{ GeV}/c^2$ .

386 the residual background and a Voigtian function (a convolution of a Breit-Wigner and a  
 387 Gaussian function accounting for the detector resolution) for the signal was used. The  
 388 mathematical form of fit function used in analysis is:

$$f(M_{\Xi\pi}) = \frac{Y}{2\pi} \frac{\Gamma_0}{(M_{\Xi\pi} - M_0)^2 + \frac{\Gamma_0^2}{4}} \frac{e^{-(M_{\Xi\pi} - M_0)/2\sigma^2}}{\sigma\sqrt{2\pi}} + bg(M_{\Xi\pi}) \quad (1)$$

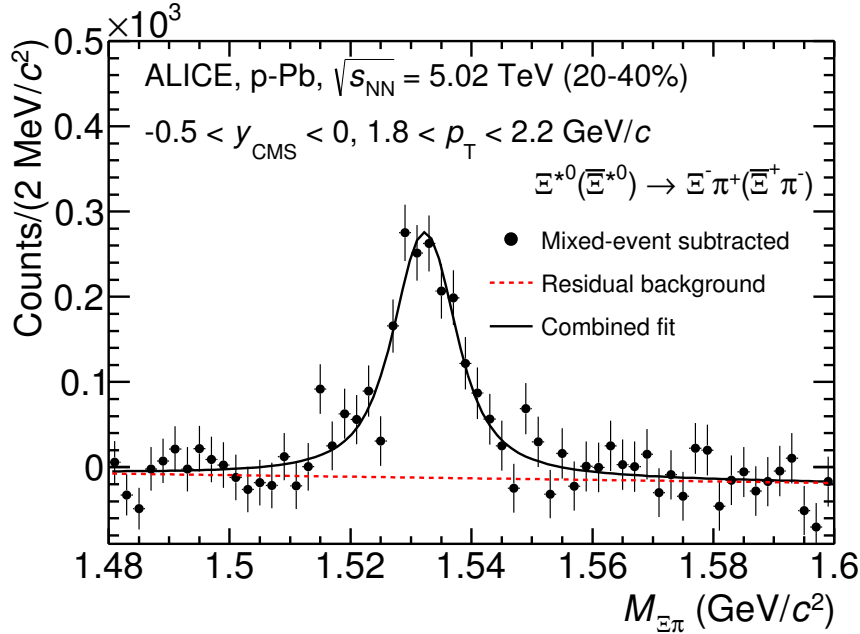


Figure 17: The invariant mass distribution after subtraction of the mixed-event background in p–Pb collisions. The solid curve represents the combined fit, while the dashed line describes the residual background.

389 The mass parameter of the Voigtian fit ( $M_0$ ) is left free within the fit range ( $1.48 \text{ GeV}/c^2$   
 390 and  $1.59 \text{ GeV}/c^2$ ). The overall invariant mass width of the Voigtian function is governed  
 391 by 2 parameters:  $\sigma$  and  $\Gamma_0$ . The  $\sigma$  describes the broadening of the peak due to finite  
 392 detector resolution while  $\Gamma$  describes the intrinsic width of the resonance itself. The  $\Gamma_0$  is  
 393 fixed to the PDG value of  $9.1 \text{ MeV}/c$  for the  $\Xi(1530)^0$ . Because of lack of statistics, the  
 394  $\sigma$  can be over estimated. Therefore the  $\sigma$  parameter is fixed to value derived from  $\sigma$  in  
 395 MB events which has largest statistics. The  $\sigma$  as function of  $p_T$  distribution in MB events  
 396 is shown in Figure. 19 and we also report invariant mass of  $\Xi(1530)^0$  as function of  $p_T$  in  
 397 Figure. 20. The  $\Xi(1530)^0$  raw yields have been extracted from the fit for the 4 multiplicity

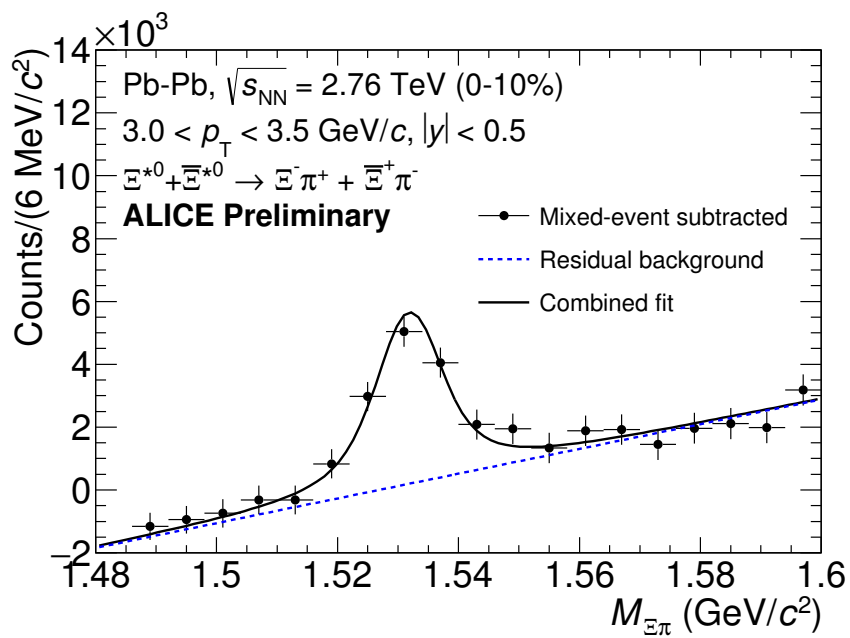


Figure 18: The invariant mass distribution after subtraction of the mixed-event background in Pb–Pb collisions. The solid curve represents the combined fit, while the dashed line describes the residual background.

<sup>398</sup> bins (+ NSD events) in p–Pb and 4 centrality bins in Pb–Pb collisions and the yields as  
<sup>399</sup> function of  $p_T$  are shown in Figure 21.

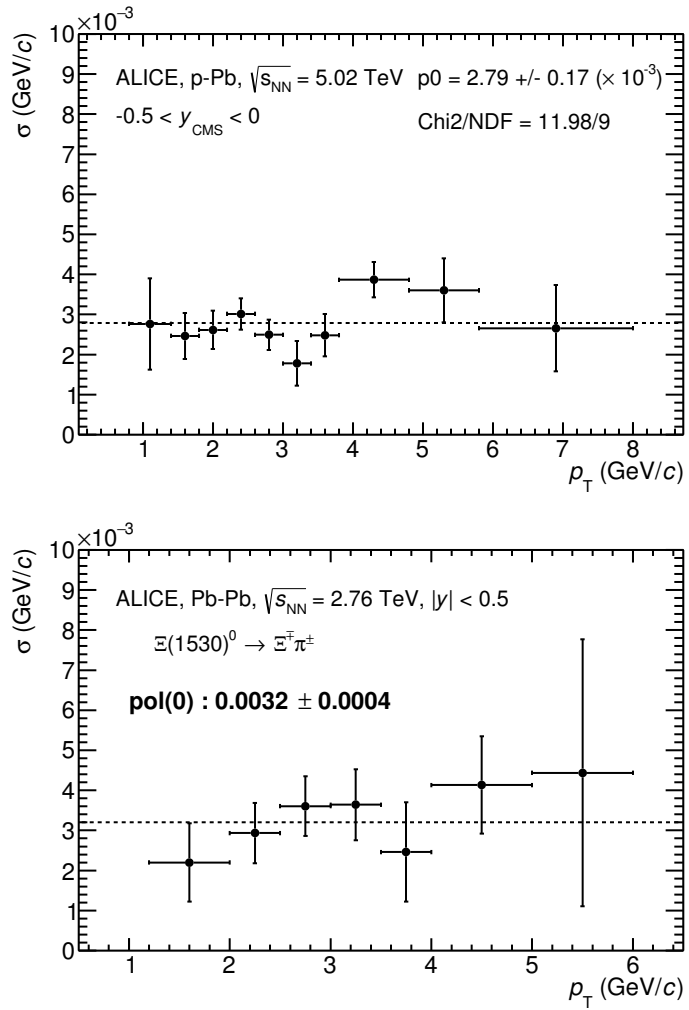


Figure 19:  $\sigma$  fit parameters as a function of  $p_T$  in MB in p–Pb collisions (top) and in Pb–Pb collisions (bottom).

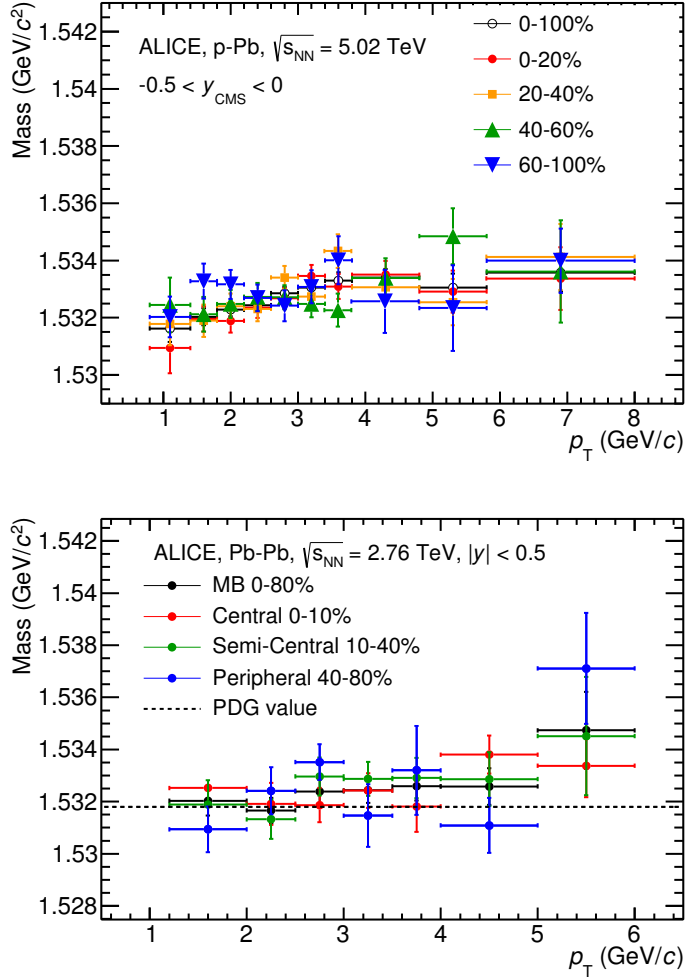


Figure 20:  $\Xi(1530)^0$ -mass obtained from fit of the Voigtian peak as a function of  $p_T$  in each multiplicity classes in p-Pb collisions (top) and the different centrality classes in Pb-Pb (bottom).

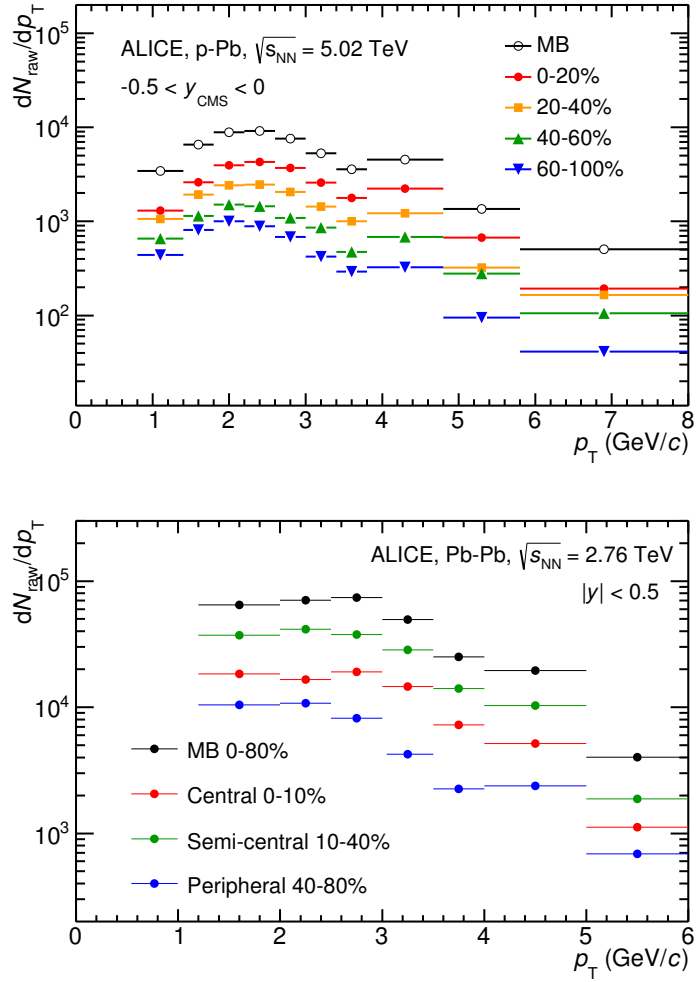


Figure 21:  $\Xi(1530)^0$  -raw spectra obtained from fit of the Voigtian peak and a polynomial residual background for different multiplicities in p-Pb collisions (top) and Pb-Pb collisions (bottom). Only the statistical error is reported.

400 **5.2 Efficiency correction**

401 The raw yields were corrected for the geometrical acceptance and the reconstruction effi-  
 402 ciency ( $A \times \epsilon$ ) of the detector (Figure. 22). By using the DPMJET 3.05 event generator [17]  
 403 and the GEANT 3.21 package [18], a sample of about 100 million p–Pb events was sim-  
 404 ulated and reconstructed in order to compute the corrections. The distributions of  $A \times \epsilon$   
 405 were obtained from the ratio between the number of reconstructed  $\Xi^{*0}$  and the number of  
 406 generated particle in the same  $p_T$  and rapidity interval. Since the correction factors for  
 407 different multiplicity classes are in agreement with those from MB events within statistical  
 408 uncertainty, the latter were used for all multiplicity classes.

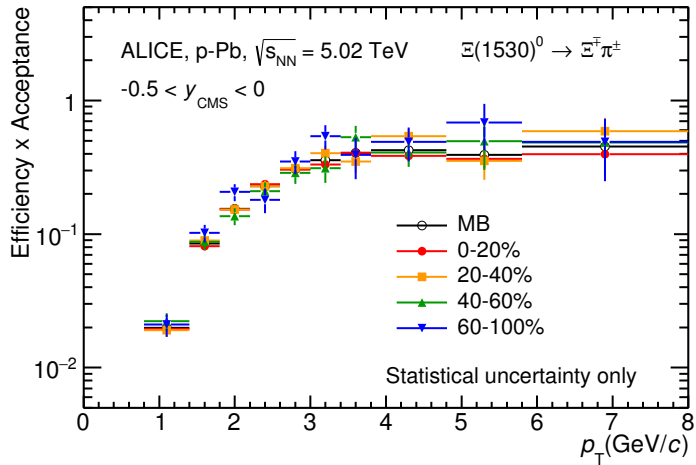


Figure 22:  $\Xi(1530)^0$  -raw spectra obtained from fit of the Voigtian peak and a polynomial residual background for different multiplicities. Only the statistical error is reported.

409 Because the generated  $\Xi(1530)^0$  spectra have different shapes than the measured  $\Xi(1530)^0$   
 410 spectra, it is necessary to weight the generated and reconstructed  $\Xi(1530)^0$  spectra in these  
 411 simulations. Fig. 23 shows the generated and reconstructed  $\Xi(1530)^0$  spectra plotted with  
 412 the (corrected) measured  $\Xi(1530)^0$  spectrum for MB events and the Levy fit of that mea-  
 413 sured spectrum. The generated and measured  $\Xi(1530)^0$  spectra have different behaviours  
 414 for the range  $0.5 < p_T < 1$  GeV/ $c$ . The generated  $\Xi(1530)^0$  spectrum decreases with  
 415 increasing  $p_T$  over this range, while the fit of the measured  $\Xi(1530)^0$  spectrum reaches a  
 416 local maximum in this range. The correction  $\epsilon$  is observed to change rapidly over this  
 417  $p_T$  range. It is therefore necessary to weight the generated spectrum so that it has the  
 418 shape of the measured  $\Xi(1530)^0$  spectrum (and to apply corresponding weights to the re-  
 419 constructed  $\Xi(1530)^0$  spectrum). An iterative procedure is performed to determine the  
 420 correct weighting (and therefore the correct  $\epsilon$ ).

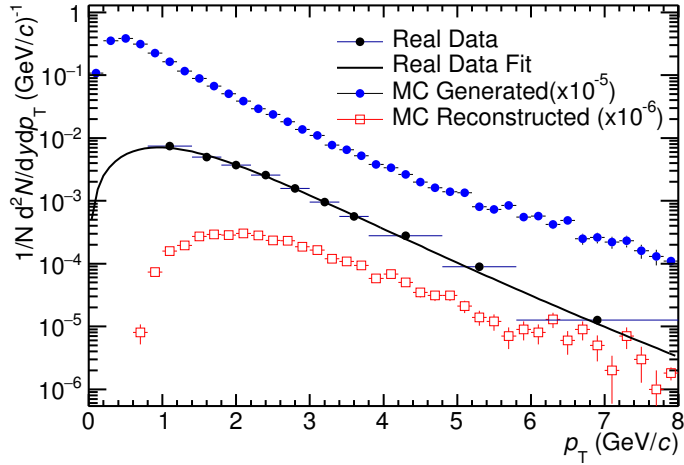


Figure 23: Real corrected  $\Xi(1530)^0$  spectrum (black) for the minimum bias with Levy fit (black curve). Also shown are the unweighted generated (blue) and reconstructed (red)  $\Xi(1530)^0$  spectra.

- 421     1. The unweighted  $\epsilon$  is calculated.
- 422     2. This  $\epsilon$  is used to correct the measured xis spectrum.
- 423     3. The corrected  $\Xi(1530)^0$  spectrum is fit.
- 424     4. This fit is used to weight the simulated xis spectra. A  $p_T$  dependent weight is applied  
425       to the generated xis spectrum so that it follows the fit. The same weight is applied  
426       to the reconstructed xis spectrum.
- 427     5. The (weighted)  $\epsilon$  is calculated.
- 428     6. Steps 2-5 are repeated (with the weighted  $\epsilon$  from step 5 used as the input for step 2)  
429       until the  $\epsilon$  values are observed to change by  $< 0.1\%$  (relative) between iterations. It  
430       is observed that four iterations are sufficient for this procedure to converge.

431     Finally, the re-weighted efficiency is obtained and the distribution as function of  $p_T$  is  
432     shown in Figure 24.

433     In order to obtain the correction factor dedicated in Pb-Pb collisions, MC events are  
434     generated using Heavy Ion Jet Interaction Generator (HIJING). The generated events are  
435     passed through a GEANT3 model of the ALICE experiment with a realistic description of  
436     the detector response. Because we have observed centrality dependent efficiency, the cen-  
437     trality dependent efficiencies have been applied to get corrected raw yield. The reweighting

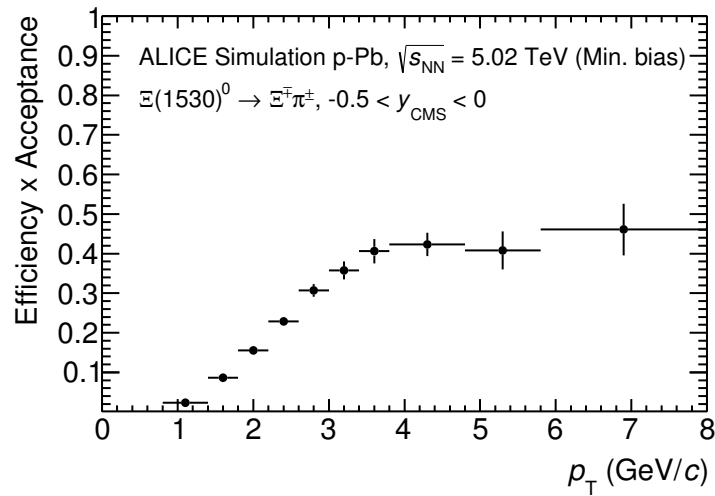


Figure 24: Efficiency as a function of  $p_T$  in minimum bias events in p–Pb collisions.

438 approach which was used to correct the efficiency in p–Pb is also applied to the efficiency  
 439 obtained in Pb–Pb.

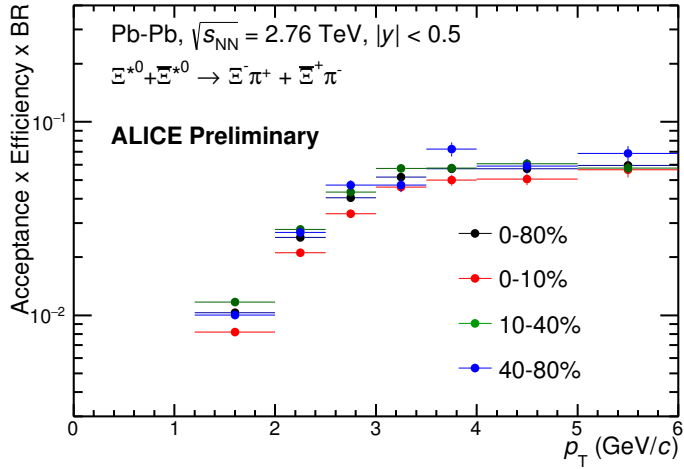


Figure 25: Efficiency as a function of  $p_T$  in different centrality classes in Pb–Pb collisions

### 440 5.3 Corrected $p_T$ -spectra

441 The  $p_T$  spectrum is by the number of produced particles of a given type in the desired  
 442 interval of phase-space divided by the number of inelastic collisions. The spectrum is  
 443 calculated as:

$$\frac{1}{N} \times \frac{d^2N}{dydp_T} = \frac{1}{N_{E,PhysSel}} \times \frac{N_{raw}}{dp_T dy} \frac{1}{\epsilon} \frac{N_{total}^{MC}}{N_{post-PVcut}^{MC}}, \quad (2)$$

444 where  $N_E$  represent the number inelastic collisions, the  $\frac{dN}{dydp_T}$  is the yield per range of  
 445 rapidity  $y$ , per range in  $p_T$ . On the right hand side  $N_{E,PhysSel}$  is the number of events  
 446 counted by the physics selection trigger.  $N_{raw}$  is the raw extracted number of particle in the  
 447 rapidity and  $p_T$  bin of width  $\Delta y = 0.5$  in p–Pb ( $\Delta y = 1.0$  in Pb–Pb) and  $\Delta p_T$ , respectively.  
 448  $\epsilon$  is the reconstruction efficiency estimated from Monte Carlo simulations.  $\frac{N_{total}^{MC}}{N_{post-PVcut}^{MC}}$  is the  
 449 ratio of the total number of particle from MC divided by the number of particle from MC  
 450 after the Primary-Vertex cut is imposed. It takes into account the fraction of particle lost  
 451 after imposing the PV cut. We notice that for minimum-bias results in p–Pb, we adopted  
 452 a normalisation such that to provide result from non-single diffractive(NSD) cross-section.  
 453 The normalisation factor is 0.964 [2]. The obtained spectrum at MB and the spectrums  
 454 from different multiplicity classes in p–Pb are shown in Figure 26 and different centrality  
 455 classes in Pb–Pb are shown in Figure 27.

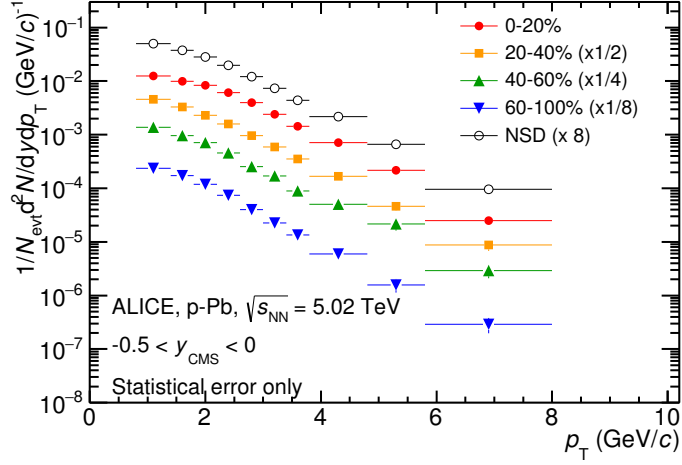


Figure 26: Corrected  $p_T$ -spectra of  $\Xi(1530)^0$  in NSD and different multiplicity classes in p–Pb collisions.

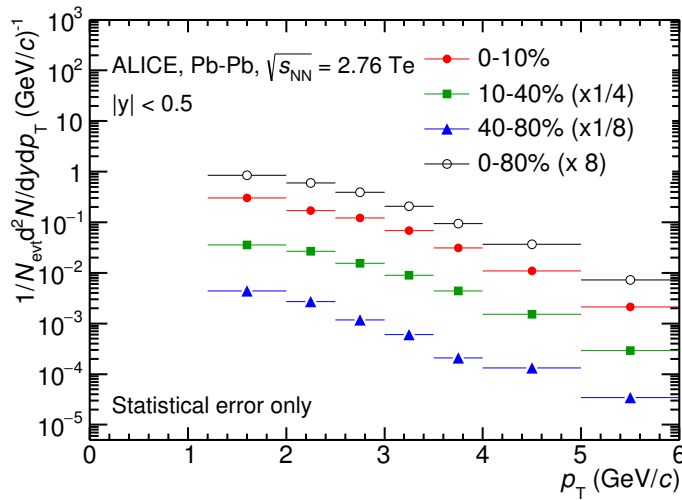


Figure 27: Corrected  $p_T$ -spectra of  $\Xi(1530)^0$  in different centrality classes in Pb-Pb collisions.

456 **5.4 Systematic uncertainties**

457 The systematic uncertainties are calculated in seven principle groups. The procedure to ob-  
458 tain the systematic uncertainties is performed many times by varying the possible permuta-  
459 tion of the analysis parameter. The general strategy for evaluating systematic uncertainties  
460 is described as following:

- 461 1. Choose one set of parameters for the analysis as default  
462 2. Observe the deviation of yield when one parameter is changed  
463 3. The systematic uncertainty is calculated for a given source as the RMS deviation of  
464 the available sources.  
465 4. The total systematic uncertainty, taking into account all the different sources, is the  
466 sum in quadrature of each source.

467 To study the systematic effect we repeat the measurement by varying one parameter at  
468 a time. A Barlow [19] check has been performed for each measurement to verify whether it  
469 is due to a systematic effect or a statistical fluctuation. Let each measurement be indicated  
470 by  $(y_i \pm \sigma_i)$  and the central value (default measurement) by  $(y_c \pm \sigma_c)$ , one can define  $\Delta\sigma_i$   
471 (Eq. 3).

$$\Delta\sigma_i = \sqrt{(\sigma_i^2 - \sigma_c^2)} \quad (3)$$

472 Then we calculate  $n_i = \Delta y_i / \Delta\sigma_i$ , where  $\Delta y_i = |y_c - y_i|$ . If  $n_i \leq 1.0$  then the effects  
473 are due to the statistical fluctuation and if  $n_i > 1.0$  we apply consistency check. Since  
474 the alternate and default measurements are not statistically independent, an alternate  
475 measurement which is statistically consistent with the default measurement should not be  
476 used in calculating a systematic uncertainty. The difference between the two measurements  
477 is  $\Delta = y_c - y_i$ . The difference in quadrature of the uncertainties is calculated by Eq. 3. It  
478 could be possible to check if  $\Delta < \sigma$  and exclude such cases from the systematic uncertainties.  
479 However, there can be statistical fluctuations for which  $\Delta > \sigma$ . If the variations between the  
480 default and alternate measurements are purely statistical, the distribution of  $\Delta/\sigma$  should  
481 be a Gaussian with a mean value that is consistent with zero and a deviation  $\sigma$  consistent  
482 with unity. In this analysis, if the mean value is less than 0.1 and  $\sigma$  is less than 1, the  
483 variation passes the consistency check.

484 Only the measurements which passed the Barlow check ( $n_i > 1$ ) are used to determine  
485 the systematic uncertainty. For measurements  $N > 2$ , the systematic uncertainty has been  
486 determined as the RMS (eqn. 4) of the available measurements. If  $N=2$ , the absolute  
487 difference is assigned as systematic uncertainty.

$$\delta y_{syst.} = \sqrt{\frac{1}{N} \sum_i (y_i - \bar{y})^2} \quad (4)$$

488 Here  $N$  is the total number of available measurements including  $y_c$  and  $\bar{y}$  is the average  
489 of value of the measurements. The measurement did not pass Barlow check, zero systematic  
490 uncertainty has been assigned to the value.

491 By suing the way as explained above, all the main contributions to the systematic un-  
492 certainty of particle spectra have been studied. In particular those that comes from signal  
493 extraction, topological and kinematical selection cuts, track quality selection and  $n\sigma$  TPC  
494 PID variation. the meaning of each source of systematic uncertainty studied is described  
495 in the following:

496

#### 497     **Signal extraction**

498 We have extracted the signal with varying the yield calculating method which contains  
499 the method of signal extraction by integrating the Voigtian fit function and bin counting.  
500 We also have varied the normalisation range which is related to the invariant mass region  
501 where the mixed events distribution is scaled to subtract the combinatorial background  
502 and different background estimator such as Like-Sign distribution and polynomial fit was  
503 taken account into the systematic source of signal extraction. The systematic uncertainty  
504 from signal extraction is sum in quadrature of three sources.

505

#### 506     **Topological selection**

507 To evaluate the stability of the chosen set of values for the topological cuts, loose and tight  
508 cuts have beed defined in order to vary by  $\pm 10\%$  respectively. The parameters are changed  
509 once at a time. Total systematic uncertainty from topological selection is calculated by  
510 summation in quadrature of nine sources.

511

#### 512     **TPC $N_{cluster}$ selection**

513 The selection performed for the daughter tracks of the cascade is that  $N_{cluster}$  is larger  
514 than 70 and the value has been varied to 60 and 80 in order to estimate the systematic  
515 uncertainty due to this selection.

516

#### 517     **TPC $dE/dx$ selection**

518 In order to evaluate any potential effect due to the TPC  $dE/dx$  selection ( $U_{PID}$ ), the  $N_\sigma$   
519 selection was varied with  $N = 2.5$  and  $3.5$ .

520

#### 521      **$p_T$ shape correction**

522 As described in Section 5.2, due to the different shape of the measured and generated  
523  $\Xi(1530)^0$  spectra, we have applied reweighing procedure to the generated spectra to have  
524 same shape and this correction is added into contributor of systematic uncertainty as  
525  $p_T$  shape correction.

526

#### 527     **Mass window range selection**

528 In order to select  $\Xi^\pm$  which is daughter particle of  $\Xi(1530)^0$ , we apply the mass window

529  $\pm 7$  MeV/ $c^2$  around  $\Xi(1530)^0$  mass on  $\Lambda\pi$  invariant mass distribution. The boundaries  
530 has been varied to  $\pm 6$  MeV/ $c^2$  and  $\pm 8$  MeV/ $c^2$  to estimate systematic uncertainty.

531

### 532     **Vertex range selection**

533 The distribution of vertex-z is shown in Fig.3. The cut on |Vz| was varied from the nominal  
534  $\pm 10$ cm to  $\pm 9$ cm,  $\pm 11$ cm.

535

### 536     **Material Budget and hadronic cross section**

537 A possible source of uncertainty comes from the description of the material, active (de-  
538 tecting area) or dead (structure and cable), that the particles cross during their travel in  
539 the MC with respect to the real material present in the detector. Such description could  
540 affect the reconstruction efficiency in different aspects (e.g. multiple scattering, energy  
541 loss). The value estimated by  $\Xi$  analysis [20] has been used in this study which gives 4%  
542 systematic uncertainty. In case of systematic uncertainty from hadronic cross section, we  
543 have inherited the value studied in previous measurement[21] which amount is 1%.

544

### 545     **Tracking efficiency**

546 Systematic uncertainties from tracking efficiency from ITS + TPC combined track were  
547 assigned as 3% in p–Pb and 4% in Pb–Pb collision system.[21]  
548 (<https://twiki.cern.ch/twiki/bin/view/ALICE/TrackingEfficiencyCharged>)

549

550 Finally, total systematic uncertainty is sum in quadrature of sources listed above. Fig-  
551 ure 28 and Figure 29 show the total systematic uncertainty in minimum bias event and  
552 different multiplicity classes in p–Pb collisions, respectively. Again, Figure 30 and Figure  
553 31 present the total systematic uncertainty in minimum bias event and different centrality  
554 classes in Pb–Pb collisions.

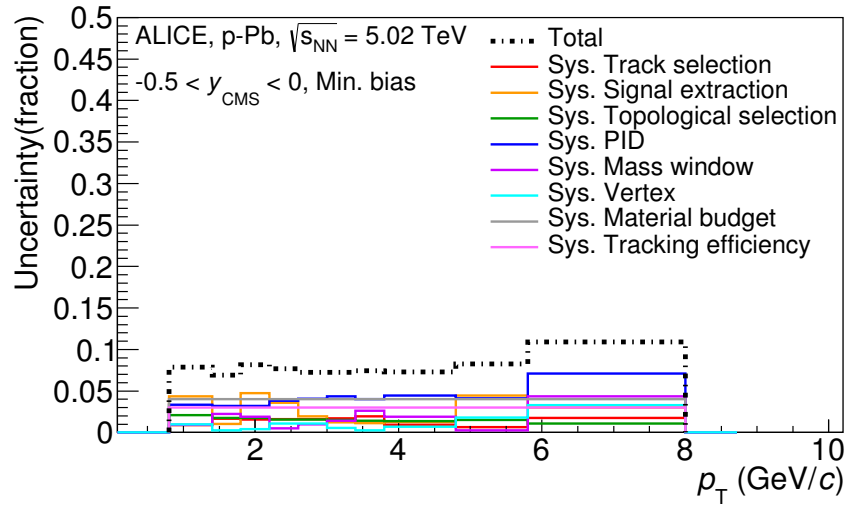


Figure 28: Summary of the contributions to the systematic uncertainty in minimum bias events in p–Pb collisions. The dashed black line is the sum in quadrature of all the contributions.

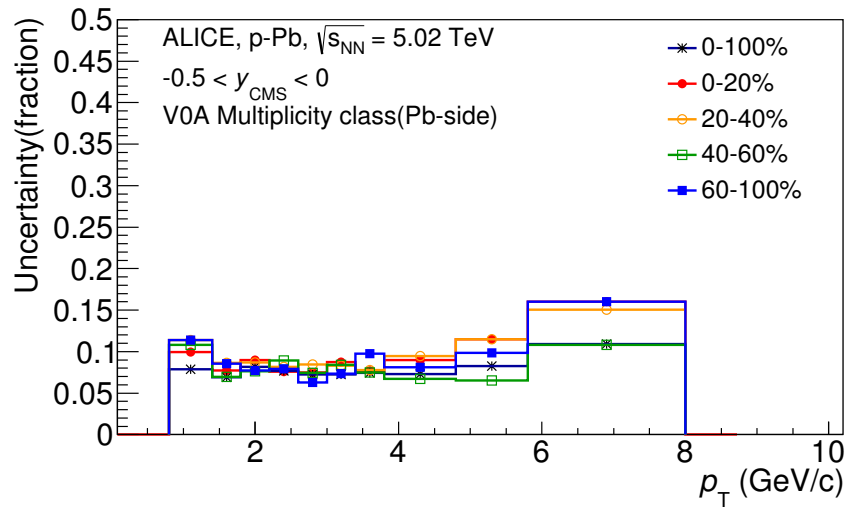


Figure 29: Systematic uncertainties for each multiplicity classes in p–Pb collisions.

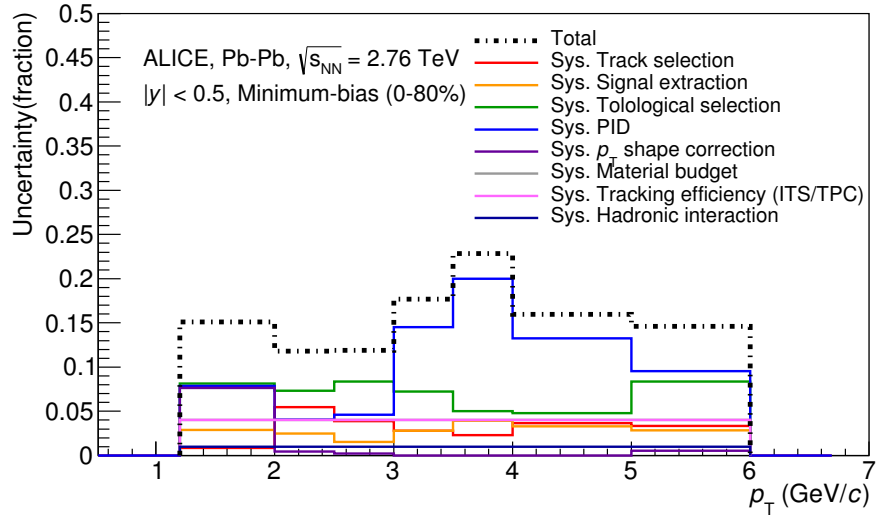


Figure 30: Summary of the contributions to the systematic uncertainty in minimum bias events in Pb–Pb collisions. The dashed black line is the sum in quadrature of all the contributions.

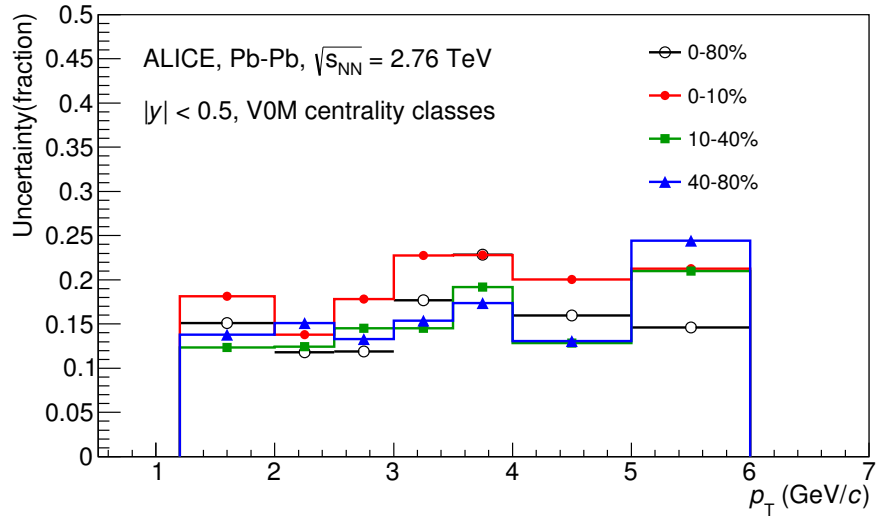


Figure 31: Systematic uncertainties for each multiplicity classes.

Source of uncertainty	$\Xi(1530)^0$ in p-Pb	$\Xi(1530)^0$ in Pb-Pb
<i>p<sub>T</sub>-dependent</i>		
Tracking efficiency	3%	4%
Tracks selection	1-2%	1-5%
Topological selection	1-2%	5-8%
PID	3-7%	4-20%
Signal extraction	1-5%	1-4%
<i>p<sub>T</sub></i> shape correction	-	0-8%
Mass window ( $\Xi^{\pm}$ )	4	-
Vertex selection	3%	-
<i>p<sub>T</sub>-independent</i>		
Hadronic interaction	-	1%
Material budget	4%	4%
Branching ratio	0.3%	0.3%
Total	8-12%	9-25 %

Table 7: Summary of the systematic uncertainties on the differential yield,  $d^2N/(dp_T dy)$ . Minimum and maximum values in all  $p_T$  intervals and multiplicity classes in p–Pb, centrality classes in Pb–Pb are shown for each source.

555    **5.5  $\Xi(1530)^0$  transverse momentum spectra**

556    The raw yield shown in Figure 26 and 27 have been corrected for efficiency as described  
 557    in section 5.2. The measured spectra for  $(\Xi(1530)^0 + \bar{\Xi}(1530)^0)/2$  are reported in Figure  
 558    32 for p–Pb collisions and Figure 33 for Pb–Pb collisions. The statistical and systematic  
 559    uncertainties are reported respectively as the error bars and the boxes on the plot. The  
 560    corrected yields for p–Pb collisions are measured with  $0.8 < p_T < 8.0$  GeV/c while the  
 561    yields for Pb–Pb collisions are obtained with  $1.2 < p_T < 6.0$  GeV/c due to difficulty of  
 562    signal extraction in low and high  $p_T$  region.

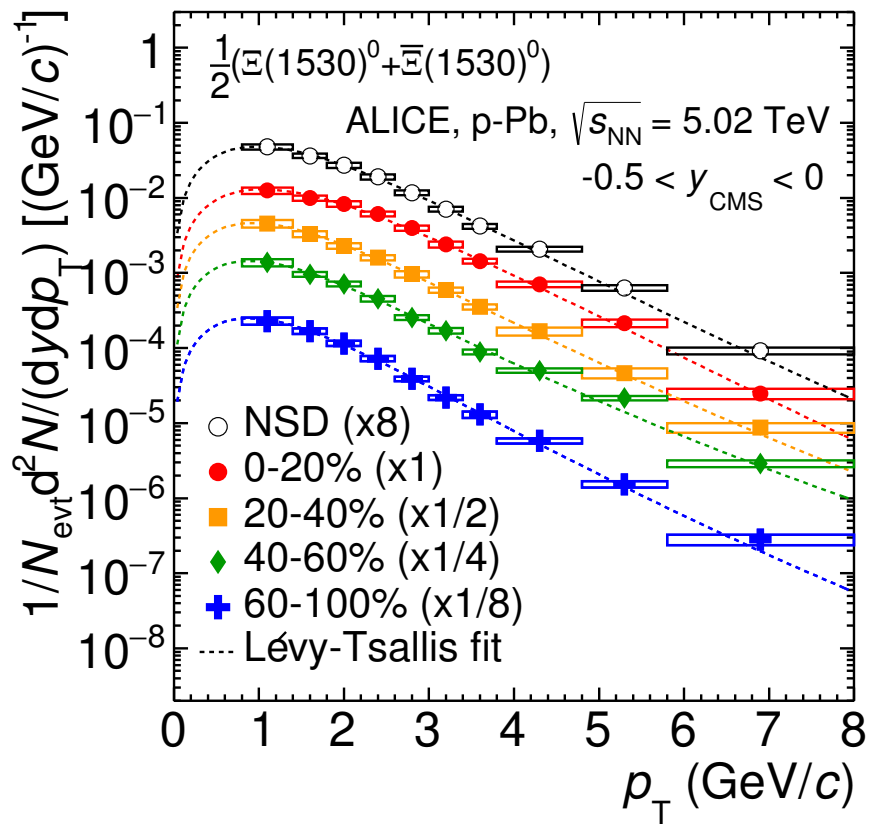


Figure 32: Corrected yields as function of  $p_T$  in NSD events and multiplicity dependent event classes in p-Pb collision system. Statistical uncertainties are presented as bar and systematical uncertainties are plotted as boxes.

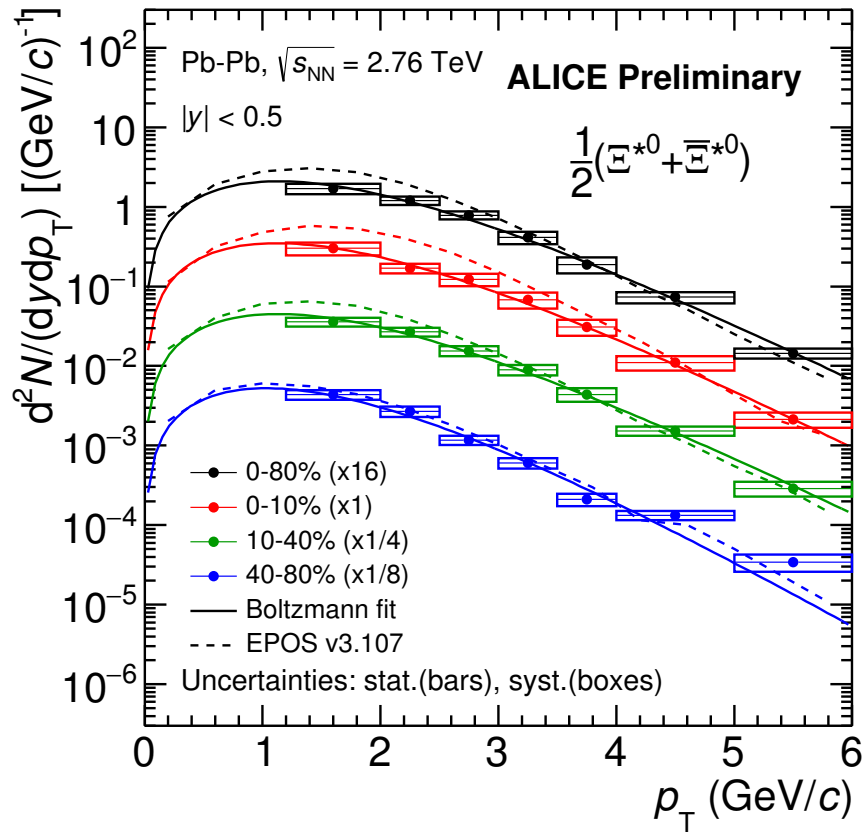


Figure 33: Corrected yields as function of  $p_T$  in different centrality classes in  $\text{Pb-Pb}$  collision system. Statistical uncertainties are presented as bar and systematical uncertainties are plotted as boxes.

563 **6 Results**

564 **6.1 Mean transverse momentum**

565 Figure 34 shows the mean transverse momentum  $\langle p_T \rangle$  as a function of mean charged-  
 566 particle multiplicity density  $\langle dN_{\text{ch}}/d\eta_{\text{lab}} \rangle$  at midrapidity. The results for  $\Xi(1530)^0$  are  
 567 compared with those for other hyperons observed in p–Pb collisions at  $\sqrt{s_{\text{NN}}} = 5.02$  TeV [1,  
 568 3].

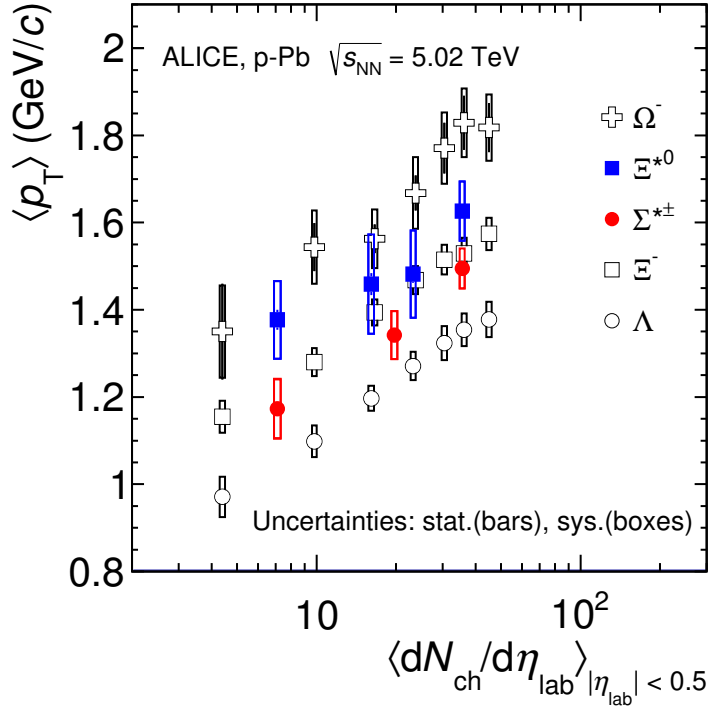


Figure 34: Mean transverse momenta  $\langle p_T \rangle$  of  $\Lambda$ ,  $\Xi^-$ ,  $\Sigma^{*\pm}$ ,  $\Xi^{*0}$  and  $\Omega^-$  in p–Pb collisions at  $\sqrt{s_{\text{NN}}} = 5.02$  TeV as a function of mean charged-particle multiplicity density  $\langle dN_{\text{ch}}/d\eta_{\text{lab}} \rangle$ , measured in the pseudorapidity range  $|\eta_{\text{lab}}| < 0.5$ . The results for  $\Lambda$ ,  $\Xi^-$  and  $\Omega^-$  are taken from [1, 2, 3]. Statistical and systematic uncertainties are represented as bars and boxes, respectively. The  $\Omega^-$  and  $\Xi^-$  points in the 3rd and 4th lowest multiplicity bins are slightly displaced along the abscissa to avoid superposition with the  $\Xi(1530)^0$  points.

569 Increasing trends from low to high multiplicities are observed for all hyperons. The  
 570 mean transverse momenta increase by 20% as the mean charged-particle multiplicity in-  
 571 creases from 7.1 to 35.6. This result is similar to the one obtained for the other hyperons.  
 572 Furthermore, a similar increase has been observed also for  $K^\pm$ ,  $K_S^0$ ,  $K^*(892)^0$  and  $\phi$  [2],

573 whereas protons are subject to a larger ( $\sim 33\%$ ) increase in the given multiplicity range,  
 574 as discussed also in Ref. [1].

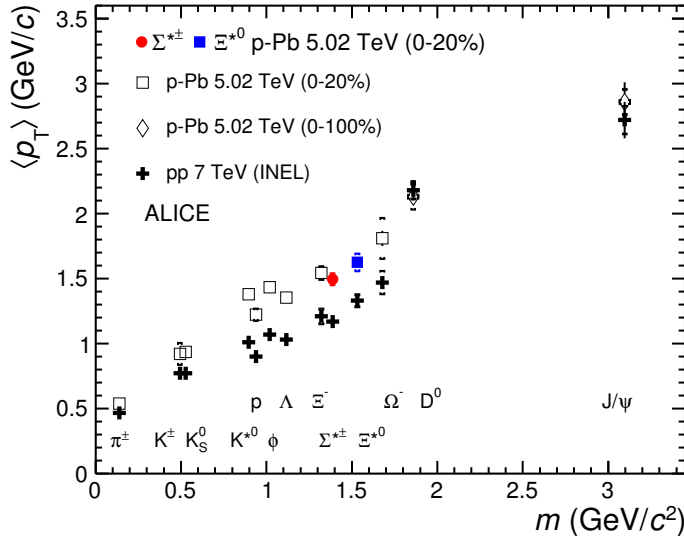


Figure 35: Mass dependence of the mean transverse momenta of identified particles for the 0 – 20% V0A multiplicity class and with  $-0.5 < y_{\text{CMS}} < 0$  in p–Pb collisions at  $\sqrt{s_{\text{NN}}} = 5.02 \text{ TeV}$  [1, 3], and in minimum-bias pp collisions at  $\sqrt{s} = 7 \text{ TeV}$  [4] with  $|y_{\text{CMS}}| < 0.5$ . Additionally,  $D^0$  and  $J/\psi$  results are plotted. The  $D^0$  and  $J/\psi$  were measured in different rapidity ranges:  $|y_{\text{CMS}}| < 0.5$  [5] ( $|y_{\text{CMS}}| < 0.9$  [6]) for  $D^0$  ( $J/\psi$ ) in pp and  $-0.96 < y_{\text{CMS}} < 0.04$  [5] ( $-1.37 < y_{\text{CMS}} < 0.43$  [7]) for  $D^0$  ( $J/\psi$ ) in p–Pb. Note also that the results for  $D^0$  and  $J/\psi$  in p–Pb collisions are for the 0-100% multiplicity class.

575 In all multiplicity classes, the  $\langle p_T \rangle$  follows an approximate mass ordering:  $\langle p_T \rangle_\Lambda <$   
 576  $\langle p_T \rangle_{\Xi^-} \simeq \langle p_T \rangle_{\Sigma^{*\pm}} < \langle p_T \rangle_{\Xi^{*0}} < \langle p_T \rangle_{\Omega^-}$ . The  $\langle p_T \rangle$  of  $\Sigma^{*\pm}$  looks systematically lower than  
 577 the  $\langle p_T \rangle$  of  $\Xi^-$ , despite the larger mass of  $\Sigma^{*\pm}$ . The uncertainties, however, are too large  
 578 to draw any conclusion on possible hints of violation of the mass hierarchy. This hierarchy  
 579 of mass-ordering, also including  $D^0$  and  $J/\psi$  in the comparison, is displayed in Figure  
 580 35. Note, however, that the  $D^0$  and  $J/\psi$  were measured in different rapidity ranges:  
 581  $|y_{\text{CMS}}| < 0.5$  [5] ( $|y_{\text{CMS}}| < 0.9$  [6]) for  $D^0$  ( $J/\psi$ ) in pp and  $-0.96 < y_{\text{CMS}} < 0.04$  [5]  
 582 ( $-1.37 < y_{\text{CMS}} < 0.43$  [7]) for  $D^0$  ( $J/\psi$ ) in p–Pb, and the results for  $D^0$  and  $J/\psi$  in p–Pb  
 583 collisions are for the 0-100% multiplicity class. This mass dependence is observed in both  
 584 p–Pb and pp collisions. It was observed also by the STAR collaboration [22] in MB pp,  
 585 MB d–Au and central Au–Au collisions.

586 Furthermore, for the light-flavour hadrons, the mean transverse momenta in p–Pb col-  
 587 lisions are observed to be consistently higher than those in pp collisions at 7 TeV. The

588 situation for the charm hadrons is different, where  $\langle p_T \rangle$  appears compatible between both  
589 colliding systems. The discrepancy is likely due to different production mechanisms for  
590 heavy and light flavours and to a harder fragmentation of charm quarks. Specifically, the  
591 fact that  $\langle p_T \rangle$  remains similar in pp and in p–Pb is consistent with an  $R_{\text{pPb}}$  ratio com-  
592 patible with unity at all  $p_T$ [5] for  $D^0$ , and/or with the effects of shadowing in p–Pb which  
593 reduces the production at low  $p_T$  and thus increasing the overall  $\langle p_T \rangle$  for  $J/\psi$  [7]; the small  
594  $p_T$ hardening expected in pp when going from 5.02 to 7TeV is apparently not enough to  
595 counter-balance the situation.

596 Because of small decrease of the  $\langle p_T \rangle$  for proton and  $\Lambda$  relative to those for  $K^{*0}$  and  
597  $\phi$ , two different trends for mesons and baryons have been suggested [23]. Even including  
598  $D^0$  and  $J/\psi$ , as shown in Figure 35, a different trend for mesons and baryons cannot be  
599 convincingly established.

## 600 6.2 Particle yield ratios

### 601 6.2.1 Comparison with other resonances

### 602 6.2.2 Comparison with models

## 603 References

- 604 [1] **ALICE** Collaboration, J. Adam *et al.*, “Multiplicity dependence of pion, kaon,  
605 proton and lambda production in p–Pb collisions at  $\sqrt{s_{\text{NN}}}= 5.02$  TeV,” *Phys. Lett.*  
606 **B728** (2014) 25–38, [arXiv:1307.6796 \[nucl-ex\]](#).
- 607 [2] **ALICE** Collaboration, J. Adam *et al.*, “Production of  $K^*(892)^0$  and  $\phi(1020)$  in  
608 p–Pb collisions at  $\sqrt{s_{\text{NN}}}= 5.02$  TeV,” *Eur. Phys. J.* **C76** (2016) 245,  
609 [arXiv:1601.7868 \[nucl-ex\]](#).
- 610 [3] **ALICE** Collaboration, J. Adam *et al.*, “Multi-strange baryon production in p–Pb  
611 collisions at  $\sqrt{s_{\text{NN}}}=5.02$  TeV,” *Phys. Lett.* **B758** (2016) 389–401,  
612 [arXiv:1512.07227 \[nucl-ex\]](#).
- 613 [4] **ALICE** Collaboration, B. Abelev *et al.*, “Production of  $\Sigma(1385)^{\pm}$  and  $\Xi(1530)^0$  in  
614 proton-proton collisions at  $\sqrt{s}= 7$  TeV,” *Eur. Phys. J.* **C75** (2015) 1,  
615 [arXiv:1406.3206 \[nucl-ex\]](#).
- 616 [5] **ALICE** Collaboration, J. Adam *et al.*, “ $D$ -meson production in p–Pb collisions at  
617  $\sqrt{s_{\text{NN}}}= 5.02$  TeV and in pp collisions at  $\sqrt{s}= 7$  TeV,” *Phys. Rev. C* **94** (2016)  
618 054908, [arXiv:1605.07569 \[nucl-ex\]](#).
- 619 [6] **ALICE** Collaboration, B. Abelev *et al.*, “Inclusive  $J/\psi$  production in pp collisions  
620 at  $\sqrt{s}= 2.76$  TeV,” *Phys. Lett.* **B718** (2012) 295–306, [arXiv:1203.3641 \[hep-ex\]](#).

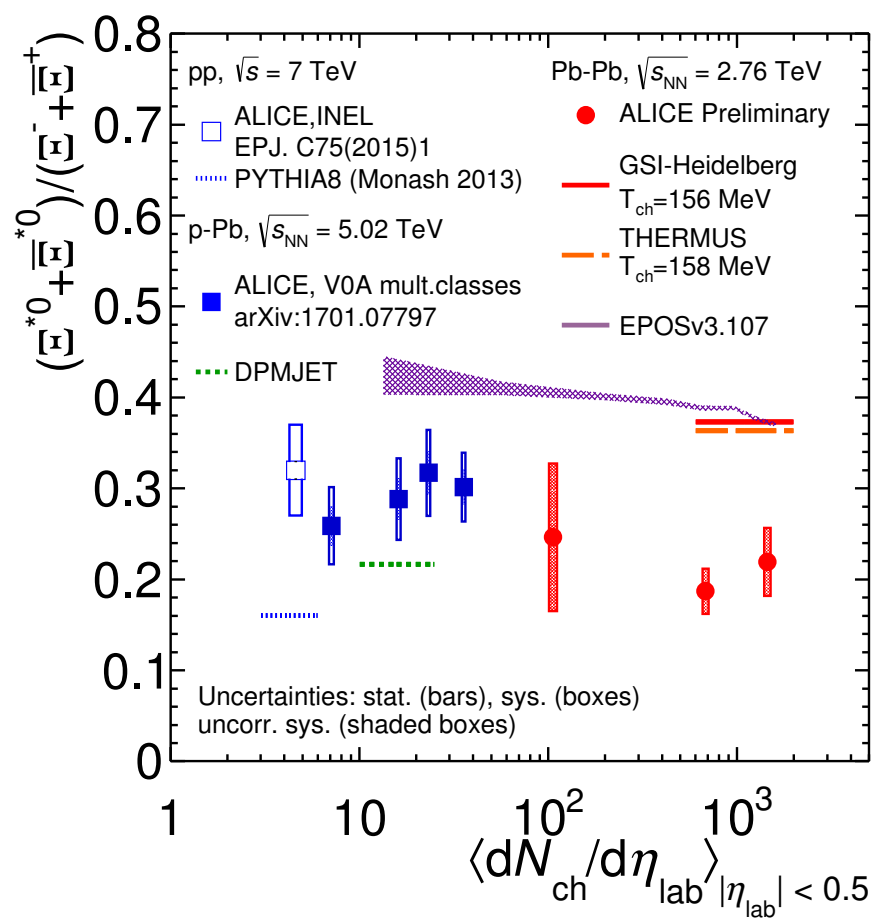


Figure 36: Integrated.

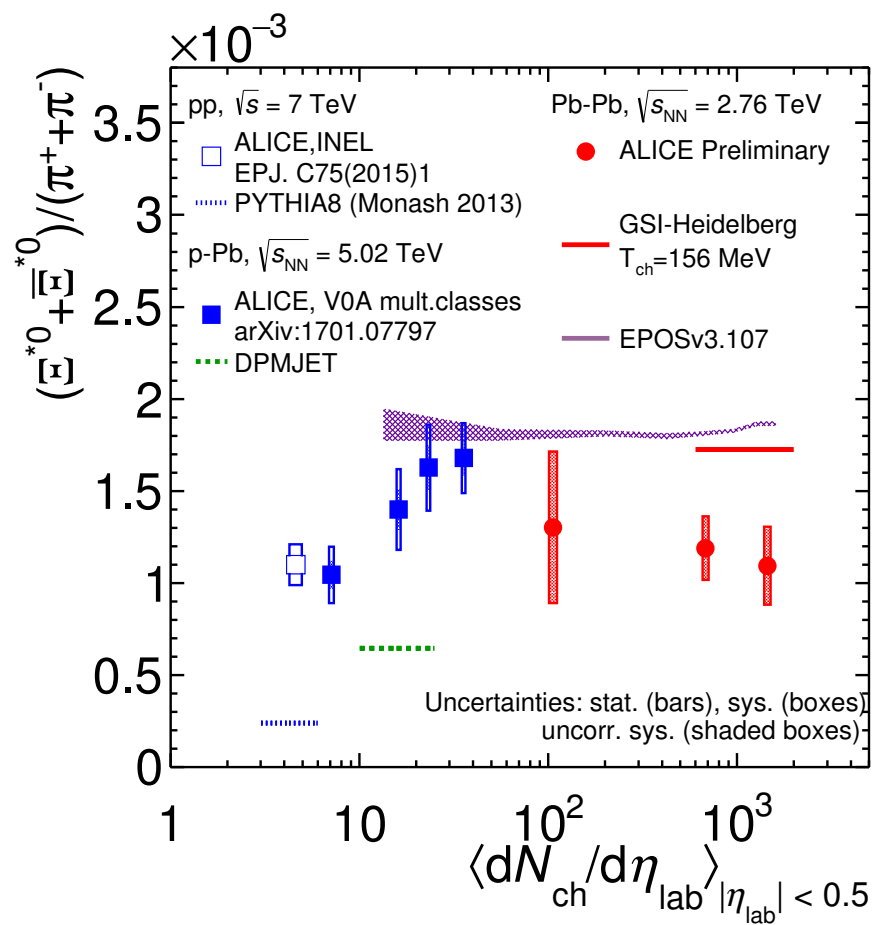


Figure 37: Integrated.

- 621 [7] **ALICE** Collaboration, J. Adam *et al.*, “Rapidity and transverse-momentum  
 622 dependence of the inclusive  $J/\psi$  nuclear modification factor in p–Pb collisions at  
 623  $\sqrt{s_{NN}} = 5.02$  TeV,” *JHEP* **06** (2015) 55, [arXiv:1503.07179 \[nucl-ex\]](#).
- 624 [8] D. Hahn and H. Stoecker, “THE QUANTUM STATISTICAL MODEL OF  
 625 FRAGMENT FORMATION: ENTROPY AND TEMPERATURE EXTRACTION  
 626 IN HEAVY ION COLLISIONS,” *Nucl. Phys.* **A476** (1988) 718–772.
- 627 [9] S. Wheaton, J. Cleymans, and M. Hauer, “THERMUS: A Thermal model package  
 628 for ROOT,” *Comput. Phys. Commun.* **180** (2009) 84–106, [hep-ph/0407174](#).
- 629 [10] J. Cleymans, S. Kabana, I. Kraus, H. Oeschler, K. Redlich, and N. Sharma,  
 630 “Antimatter production in proton-proton and heavy-ion collisions at ultrarelativistic  
 631 energies,” *Phys. Rev.* **C84** (2011) 054916, [arXiv:1105.3719 \[hep-ph\]](#).
- 632 [11] **ALICE** Collaboration, K. Aamodt *et al.*, “The ALICE experiment at the CERN  
 633 LHC,” *JINST* **3** (2008) S08002.
- 634 [12] **ALICE** Collaboration, B. Abelev *et al.*, “Performance of the ALICE Experiment at  
 635 the CERN LHC,” *Int. J. Mod. Phys.* **A29** (2014) 1430044, [arXiv:1402.4476](#)  
 636 [nucl-ex].
- 637 [13] **ALICE** Collaboration, B. Abelev *et al.*, “Pseudorapidity Density of Charged  
 638 Particles in p–Pb Collisions at  $\sqrt{s_{NN}} = 5.02$  TeV,” *Phys. Rev. Lett.* **110** (2013)  
 639 032301, [arXiv:1210.3615 \[nucl-ex\]](#).
- 640 [14] **ALICE** Collaboration, B. Abelev *et al.*, “Centrality determination of Pb–Pb  
 641 collisions at  $\sqrt{s_{NN}} = 2.76$  TeV with ALICE,” *Phys. Rev.* **C88** (2013) ,  
 642 [arXiv:1303.0737 \[nucl-ex\]](#).
- 643 [15] **Particle Data Group** Collaboration, K. Olive *et al.*, “Review of Particle Physics,”  
 644 *Chin. Phys.* **C38** (2014) 090001.
- 645 [16] **ALICE** Collaboration, K. Aamodt *et al.*, “Strange particle production in  
 646 proton-proton collisions at  $\sqrt{s} = 0.9$  TeV with ALICE at the LHC,” *Eur. Phys. J.*  
 647 **C71** (2011) 1594, [arXiv:1012.3257 \[nucl-ex\]](#).
- 648 [17] S. Roesler, R. Engel, , and J. Ranft, “The Monte Carlo Event Generator  
 649 DPMJET-III, Advanced Monte Carlo for Radiation Physics, Particle Transport  
 650 Simulation and Applications,” *Conference Proceedings, MC2000, Lisbon, Portugal,*  
 651 *October 23-26* (2000) 1033–1038, [hep-ph/0012252](#).
- 652 [18] R. Brun, F. Carminati, and S. Giani, “GEANT detector description and simulation  
 653 tool,” *CERN-W5013* (1994) .

- 654 [19] R. Barlow, “Systematic Errors: Facts and Fictions,” *Presented at Advanced*  
655     *Statistical Techniques in HEP, Durham, March 2002* (2002) 333p,  
656     [hep-ex/0207026v1](#).
- 657 [20] **ALICE** Collaboration, B. Abelev *et al.*, “Multi-strange baryon production at  
658     mid-rapidity in Pb–Pb collisions at  $\sqrt{s_{\text{NN}}}= 2.76 \text{ TeV}$ ,” *Phys. Lett.* **B728** (2014)  
659     216–227, [arXiv:1307.5543 \[nucl-ex\]](#).
- 660 [21] **ALICE** Collaboration, B. Abelev *et al.*, “Centrality dependence of  $\pi$ ,  $K$  and  $p$   
661     production in Pb–Pb collisions at  $\sqrt{s_{\text{NN}}}= 2.76 \text{ TeV}$ ,” *Phys. Rev.* **C88** (2013) ,  
662     [arXiv:1301.4361 \[nucl-ex\]](#).
- 663 [22] **STAR** Collaboration, B. I. Abelev *et al.*, “Hadronic resonance production in d–Au  
664     collisions at  $\sqrt{s_{\text{NN}}}= 200 \text{ GeV}$  measured at the BNL Relativistic Heavy-Ion Collider,”  
665     *Phys. Rev.* **C78** (2008) 044906, [arXiv:0801.0450 \[nucl-ex\]](#).
- 666 [23] A. Velásquez, “Mean  $p_{\text{T}}$  scaling with  $m/n_q$  at the LHC: Absence of (hydro) flow in  
667     small systems?,” *Nucl. Phys.* **A943** (2015) 9–17, [arXiv:1506.00584 \[hep-ph\]](#).

668 **Acknowledgements**